Analysis of Non-Oberbeck-Boussinesq effects on turbulent Rayleigh-Bénard convection in a liquid

A numerical study

Lucas C. Buijs

Technische Universiteit Delft

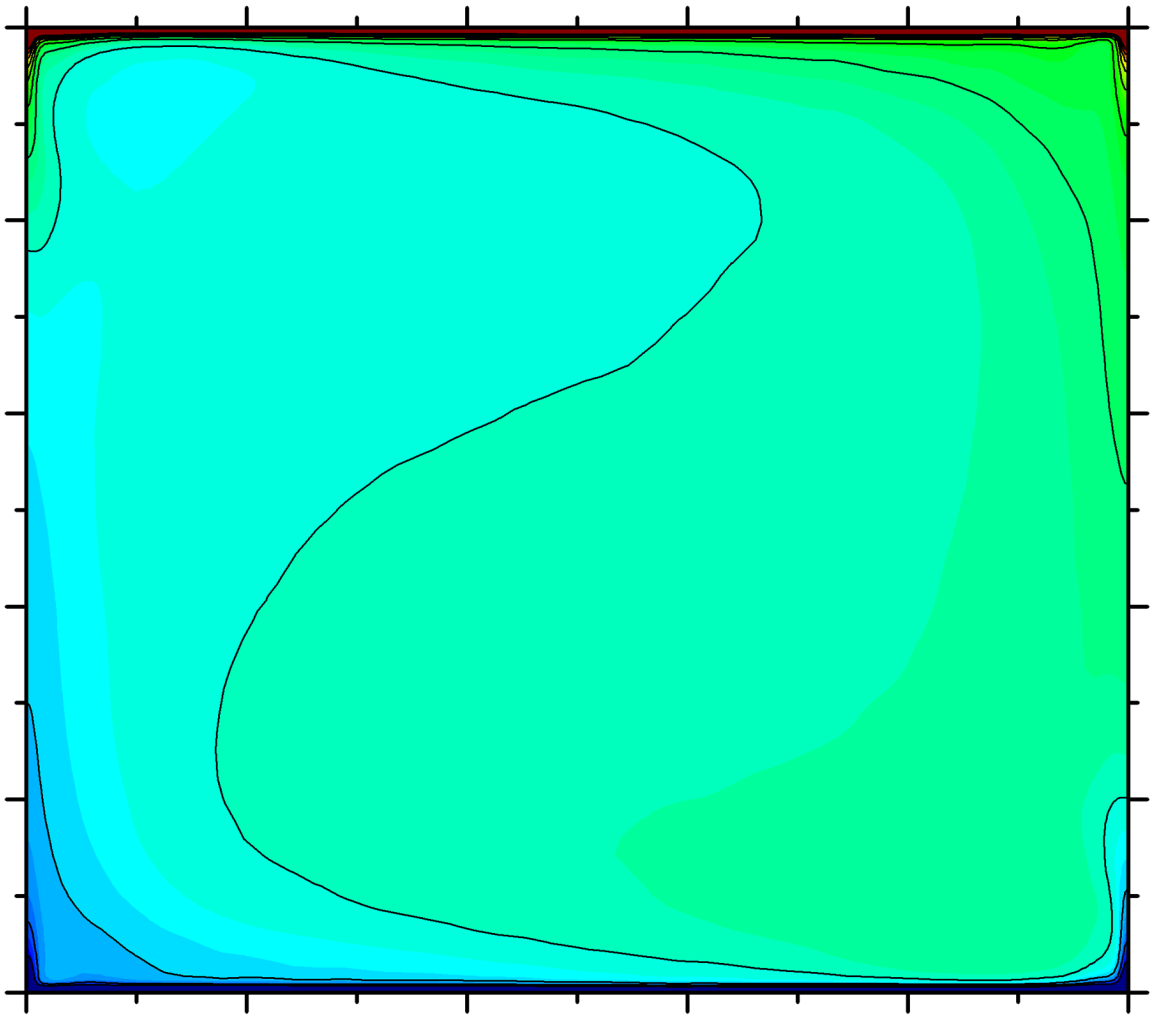

TU Delft Delft University of Technology

Challenge the future

Analysis of Non-Oberbeck-Boussinesq effects on turbulent Rayleigh-Bénard convection in a liquid

A numerical study

by

Lucas C. Buijs

in partial fulfillment of the requirements for the degree of

Master of Science
in Applied Physics

at the Delft University of Technology,
to be defended on Tuesday September 29, 2015 at 10:00 AM.

Supervisors:	Ir. J.W.R. Peeters,	TU Delft
	Prof. dr. ir. B. J. Boersma,	TU Delft
	Dr. M. Rohde,	TU Delft
Thesis committee:	Ir. J.W.R. Peeters,	TU Delft
	Prof. dr. ir. B. J. Boersma,	TU Delft
	Dr. M. Rohde,	TU Delft
	Dr. ir. J. L. Kloosterman,	TU Delft

TU Delft Delft University of Technology

ABSTRACT

The influence of significant viscosity variations on turbulent Rayleigh-Bénard convection is studied, by means of direct numerical simulation of fluids in a cubical cavity. A comparison is made at Ra = 10^7 between two cases, one of which exhibits viscosity variations of the order ±20%. It is shown that the viscosity variations are on average mostly confined to the thin thermal boundary layers at the top and bottom walls of the enclosure. They induce a downward displacement of the mean velocity profile, because the velocity gradient magnitude is increased at the bottom wall and increased at the top wall. This also increases the production of turbulent kinetic energy at the bottom wall and decreases it at the top wall, which results in increased fluid motion through the vertical centerplane of the cavity. The volume-averaged turbulent kinetic energy is increased by 2.87%, and the volume-averaged mean kinetic energy is increased by 0.57%. Because the bulk flow is displaced towards the bottom wall, more heat diffuses into the bulk from below, and less diffuses upwards from the bulk to the top wall. This results in an increased temperature of the bulk. The total heat flux through the system is increased by 0.9%. A comparison is also made between a case at Ra = 6.74×10^8 and a case at Ra = 6.74×10^8, the latter of which exhibits viscosity variations of ±44%. Similar changes are observed, although no significant symmetry breaking is induced by changes in the distribution of turbulent kinetic energy and mean kinetic energy. Heat transfer is increased by 0.3%, from which it can be concluded that the net positive effect of viscosity variations on heat transfer is negligible. It is deduced that the increased heat transfer due to viscosity variations is most likely caused by the symmetry breaking in the distribution of TKE, and that this effect is reduced as the Rayleigh number increases, but further investigation is necessary to verify this.

NOMENCLATURE

SYMBOLS

Symbol	Quantity	Unit
c	Velocity of sound	$\mathrm{m\,s^{-1}}$
c_p	Specific heat capacity	$\mathrm{J\,kg^{-1}\,K^{-1}}$
d^*	Grid spacing	m
f_i	Body force	N
E	Mean kinetic energy	J
e	Turbulence kinetic energy	J
g	Gravitational accelleration	$\mathrm{m\,s^{-2}}$
H	Cavity height	m
h	Specific enthalpy	J
i, j, k,	Cartesian indices	-
N	Number of grid cells	-
P	Production of TKE	W
p	Pressure	$\mathrm{N\,m^{-2}}$
q	Heat flux	$\mathrm{W\,m^{-2}}$
S_{ij}	Rate of strain tensor	$\mathrm{s^{-1}}$
T	Temperature	K
t	Time	s
u, v, w	Cartesian velocity components	$\mathrm{m\,s^{-1}}$
x, y, z	Cartesian coordinates	m

GREEK SYMBOLS

Symbol	Quantity	Unit
α	Thermal diffusivity	$\mathrm{m^2\,s^{-1}}$
β	Thermal expansivity	$\mathrm{K^{-1}}$
Δ	Difference operator	-
δ	Boundary layer thickness	m
δ_{ij}	Kronecker delta	-
ϵ	Viscous dissipation rate	W
η	Kolmogorov length scale	m
η_T	Batchelor length scale	m
ϵ	Thermal dissipation rate	W
λ	Thermal conductivity	$\mathrm{W\,m^{-1}\,K^{-1}}$
μ	Dynamic viscosity	$\mathrm{kg\,m^{-1}\,s^{-1}}$
ν	Kinematic viscosity	$\mathrm{m^2\,s^{-1}}$
ρ	Density	$\mathrm{kg\,m^{-3}}$
ρ_0	Reference density	$\mathrm{kg\,m^{-3}}$
ρ_k	Normalized density	-
τ_{ij}	Stress tensor	$\mathrm{kg\,m^{-2}\,s^{-3}}$
Φ	Arbitrary quantity	-

DIMENSIONLESS QUANTITIES

Symbol	Quantity	Definition
x^*, y^*, z^*	Normalized coordinates	x_i / H
u^*, v^*, w^*	Normalized velocity components	$u_i H / \alpha$
t^*	Normalized time	$t\alpha / H^2$
T^*	Normalized temperature	$(T - T_0)/\Delta T$
p^*	Normalized pressure	$pH^2/(\rho_0 \alpha^2)$
h^*	Dimensionless grid spacing	h/H
C	Courant number	$\Delta t \frac{u_i}{\Delta x_i}$
Gr	Grashof number	$\frac{g\beta\Delta T H^3}{\nu^2}$
Nu	Nusselt number	$\frac{qH}{\lambda\Delta T}$
Ma	Mach number	u/c
Pr	Prandtl number	$\frac{\nu}{\alpha}$
Ra	Rayleigh number	$\frac{g\beta\Delta T H^3}{\nu\alpha}$

ABBREVIATIONS

Abbreviation	Meaning
BL	Boundary layer
CFD	Computational fluid dynamics
DNS	Direct numerical simulation
LSC	Large scale circulation
OB	Oberbeck-Boussinesq
NOB	Non-Oberbeck-Boussinesq
RB	Rayleigh-Bénard
SC	Supercritical
TKE	Turbulent kinetic energy

PREFACE

A notable disadvantage of conducting a simulation project, is that there is a lot of waiting time involved. Seeing as my time in Delft has almost come to an end, I have spent a lot of that waiting time thinking about what I enjoyed so much about studying physics. I've come to recognize that, apart from helping us unravel fascinating aspects of nature, physics teaches us how to solve complex problems in an analytical way. I think that like me, many other physics students simply enjoy the challenge of such a puzzle and will keep seeking that challenge throughout the rest of their careers and lives. In the scenario that one day, I will not be working in the field of physics anymore, I will still profit from all of the problem-solving skills that my time at the Delft University has taught me. More importantly even, living in Delft has been an important learning experience in general, and I have had the great pleasure of making a lot of new friends here. I will always look back on my choice to move here and study physics as one of the best choices of my life.

ACKNOWLEDGEMENTS

I would like to thank everyone who has contributed to this project. First of all, my direct supervisor Jurriaan Peeters, who is a PhD.-researcher at the department where this research was conducted, has helped me on an almost daily basis. In doing so, he has invested a lot of time and effort, which I am very grateful for. I would also like to thank my other supervisors, professor Bendiks Jan Boersma and dr. Martin Rohde. They have presented me with the opportunity to conduct this investigation in the first place, and have regularly given me great advice. I owe gratitude to PhD.-researcher Valentina Valori, for being able to use her data for comparison. Finally, I would like to thank all the other students and the staff at the Process & Energy department, for making my stay a very pleasant one. I would wholeheartedly recommend this department to any other student looking for a thesis project.

Lucas C. Buijs
Delft, September 2015

CONTENTS

1

INTRODUCTION

One of the biggest challenges in engineering today, is to come up with practical solutions to the limited availability of resources for electricity generation. In that regard, efficiency is becoming an increasingly important factor in reactor designs. Meanwhile, reactor safety and waste management have always been always key considerations in the design process. To help overcome these challenges with the help of new concepts in nuclear energy, an international collaboration known as the Generation IV International Forum (GIF) was founded in 2001. From a large number of submitted new reactor designs, the GIF selected the six most promising designs for further investigation, one of which was the Supercritical Water Reactor (SCWR, see figure 1.1). SCWR concepts are designed to operate above the thermodynamic critical point of (light) water, giving rise to several significant advantages when compared to conventional water-cooled reactors [1]:

- A thermal efficiency of up to 44% is possible, compared to up to 36% for current reactors.
- There is no need for steam generators or steam separators and dryers.
- Higher steam enthalpy allows for a more compact turbine system.

An SCWR reactor core can be designed to operate in either the thermal or fast-neutron spectrum. The combination of these characteristics allows for both a decrease in capital costs for a given electric power output, and better fuel utilization, yielding an economic advantage in comparison with current light water reactors. There are however, significant challenges in both the prediction and utilization of heat transfer through supercritical water in general.

1.1. SUPERCRITICAL FLUIDS

For a given fluid, kept at a constant pressure greater that its critical point, the transition from a liquid-like state to a vapor-like state is a continuous process (Yoo [2]). This means that there is a continuous but drastical change in density, as well as other fluid properties, over a narrow temperature range across the pseudocritical temperature (see figure 1.2).

As mentioned in the previous section, there are significant advantages in utilizing heat transfer through supercritical fluids. One of these advantages is the increased specific enthalpy that can be observed in the figure, and allows for the downscaling of turbine systems. The characteristic thermophysical properties of supercritical fluids impose challenges as well, especially in depressurization from supercritical to sub-critical conditions. Hotspots in the reactor core can result in drastic local expansion of the coolant when near the pseudocritical temperature, which poses a direct risk of damage to the fuel. Computational fluid dynamics (CFD) codes are a valuable tool in predicting heat transfer to fluids, including supercritical fluids used in new reactor designs such as the SCWR. Many conventional CFD codes utilize the Oberbeck-Boussinesq (OB) approximation as a means to simplify calculations for convection in the coolant. This approximation only allows for small variations in the thermophysical properties of the fluids, and therefore does not apply to fluids near the pseudocritical temperature. In addition, the numerical resolution that is required for correctly conducting CFD simulations, scales with the Prandtl number of the fluid. As the specific heat capacity shows a peak at the pseudocritical temperature, so does the local Prandtl number. Therefore, CFD analysis of fluids near the pseudocritical temperature requires a much higher numerical resolution, further complicating the prediction of heat transfer in said fluids [1].

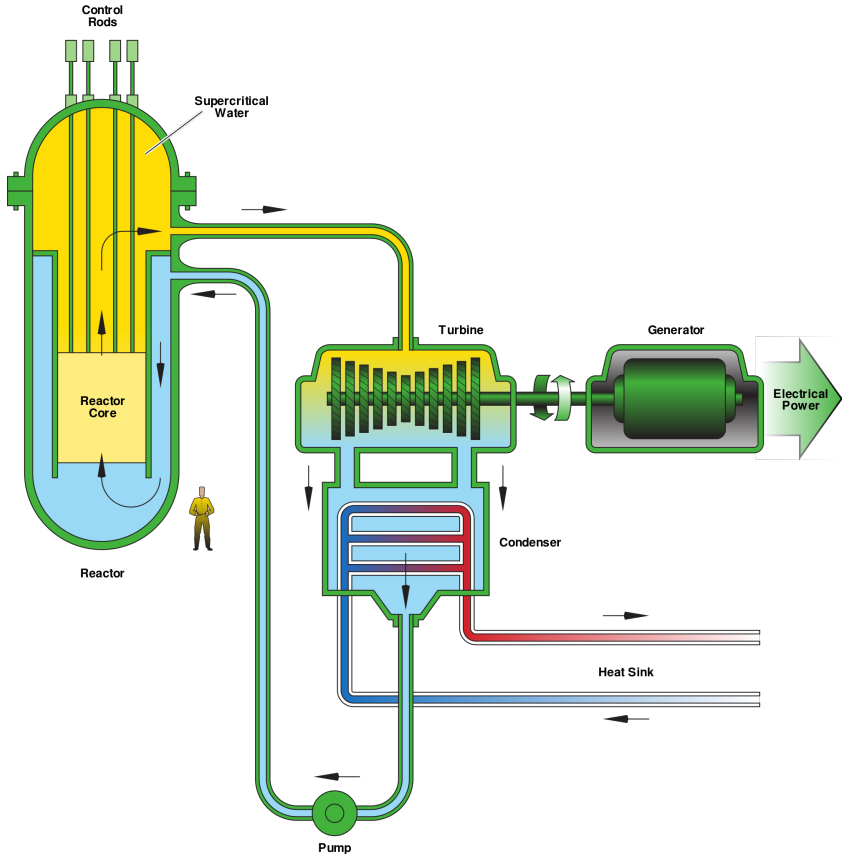

Figure 1.1: Schematic representation of the Supercritical Water Reactor concept design [1].

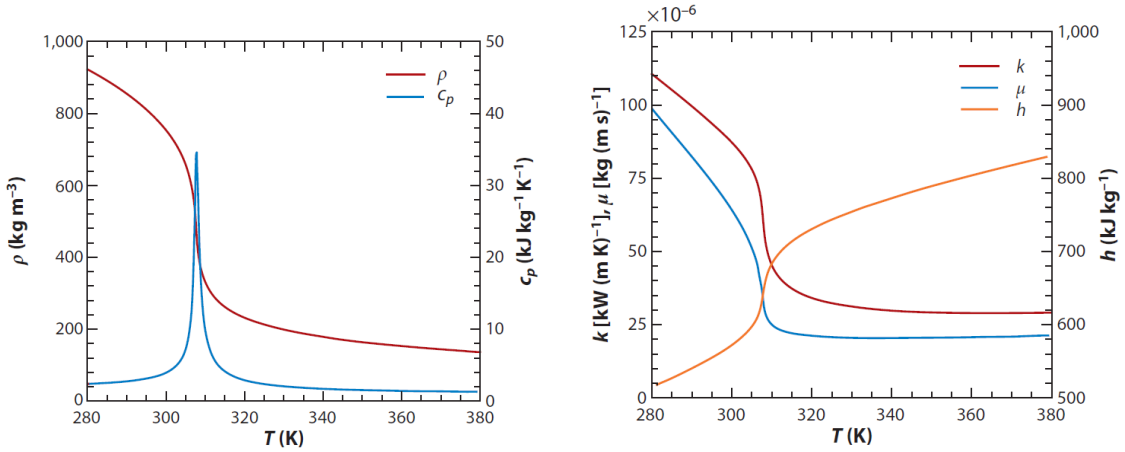

(a) Density and heat capacity of CO_2.

(b) Thermal conductivity, dynamic viscosity and specific enthalpy of CO_2.

Figure 1.2: Some thermophysical properties of CO_2 versus temperature at $P = 8$ MPa, courtesy of Yoo [2].

1.2. RESEARCH OBJECTIVES

In a nuclear reactor, heat transfer through the coolant mainly occurs by means of a combination of turbulent forced convection driven by pumps, and turbulent Rayleigh-Bénard (RB) convection. Therefore, an accurate description of each of these two components is essential to correctly predict the behaviour of the coolant. As was mentioned above, using a supercritical coolant poses significant additional challenges in the calculations that are involved. From the combination of these challenges, three main aspects can be discerned:

- The influence on fluid motion and heat transfer of variations in temperature-dependent thermophysical properties in general.
- The influence on fluid motion and heat transfer of the drastic property changes in the regime around the supercritical point.
- Local extrema in the Prandtl number imposing the requirement of greatly increased resolution.

This investigation is concerned with predicting the first of these aspects (the influence of variations in thermophysical properties), for the case of RB convection only. Therefore the overall aim of this project is:

"To aid in the understanding of the influence of variations in temperature-dependent thermophysical properties on fluid motion and heat transfer in turbulent free convection."

The investigation is conducted by means of direct numerical simulation (DNS). A well-known reference problem is chosen, namely that of turbulent RB convection in a cubical cavity heated from below. This geometry allows for a straightforward validation of the code because data from literature is available for comparison, as well a simplistic environment in which the isolated influence of the temperature-dependent fluid properties can be easily studied. To ensure a structured approach, a number of measurable research objectives was formulated:

- Goal 1: Simulate laminar free convection under OB circumstances and validate.
- Goal 2: Simulate turbulent free convection under OB circumstances and validate.
- Goal 3: Simulate laminar free convection under non-OB circumstances and validate.
- Goal 4: Simulate turbulent free convection under non-OB circumstances and validate.
- Goal 5: Investigate the influence of variations in viscosity on the mean flow and heat transfer.
  - Explain what mechanism causes significant variations in viscosity to induce a change in terms of total heat transfer.
  - Explain why this influence is reduced when the Rayleigh number is increased.

1.3. THESIS OUTLINE

In the next chapter, the reader is presented with the theory that is necessary to understand the concept of turbulent RB convection as treated in this report, along with an overview of useful background literature. Chapter 3 provides a detailed explanation of the simulation method. A validation of the code is presented in chapter 4. Subsequently, the results and their discussion are presented in chapter 5, followed by the conclusions and recommendations for future research in chapter 6.

2

THEORY

In this chapter, the reader is presented with the theory that is necessary to understand the concepts treated in this investigation. Subsequently, a short overview of related earlier research is presented.

2.1. RAYLEIGH-BÉNARD CONVECTION IN A CAVITY

Rayleigh-Bénard (RB) convection is the gravitationally driven flow that is observed between two horizontal plates, when the bottom plate is heated and the top plate is cooled. The heating and cooling of the fluid at the plates induces density differences and thus differences in the gravitational force, which in turn can lead to a net force on a fluid parcel. This investigation is concerned with RB convection in a closed cubical cavity, with the bottom plate kept at a constant temperature T_b, and the top plate at constant temperature T_t (see figure 2.1). All of the walls are rigid and stationary.

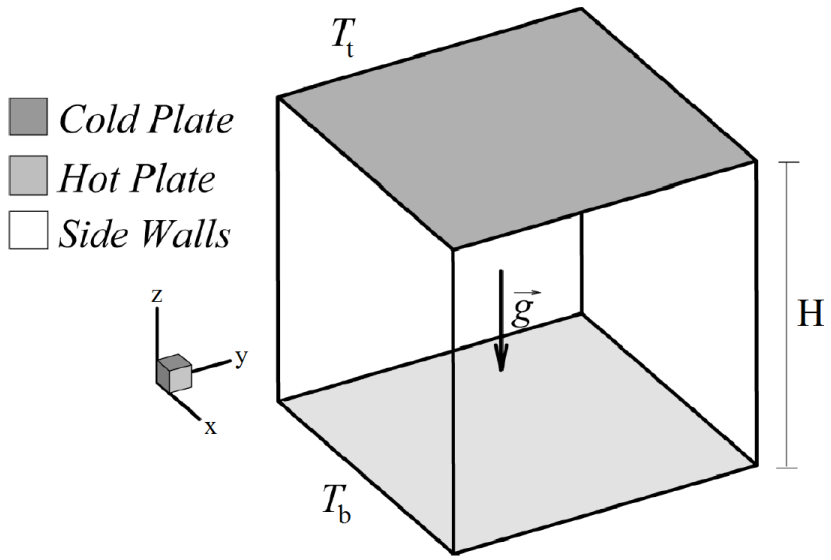

Figure 2.1: Schematic representation of the simulated cubical cavity, taken from Valencia *et al.* [3].

2.1.1. GOVERNING EQUATIONS

As is the case with many problems in fluid dynamics, this situation can be described by an application of the (local) continuity and momentum balance equations, which are (see Bird *et al.* [4]):

$$\frac{\partial \rho}{\partial t} + \frac{\partial}{\partial x_j}(\rho u_j) = 0, \tag{2.1}$$

$$\rho\left(\frac{\partial u_i}{\partial t} + u_j \frac{\partial u_i}{\partial x_j}\right) = -\frac{\partial p}{\partial x_i} + \frac{\partial \tau_{ij}}{\partial x_j} + f_i. \tag{2.2}$$

In these equations we use ρ for density, u_i for the velocity components (in Cartesian coodinates, and SI units). The terms on the left-hand side of either equation represent time rate of change and convective transport, whereas the terms on the right-hand side of the momentum equation represent production of momentum through internal stress and external body forces. The stress tensor τ_{ij} is given by:

$$\tau_{ij} = 2\mu S_{ij},$$
$$S_{ij} = \frac{1}{2}\left(\frac{\partial u_i}{\partial x_j} + \frac{\partial u_j}{\partial x_i}\right) - \frac{1}{3}\frac{\partial u_k}{\partial x_k}\delta_{ij},$$

where p is the pressure, S_{ij} is the strain rate tensor, and μ is the dynamic viscosity. For incompressible flow, the third term in the strain rate tensor can be neglected. The body forces term f_i accounts for external forces such as Coriolis, electromagnetic and gravitational forces. In the case of RB convection, we are mainly concerned with the gravitational force:

$$f_i = -\rho \begin{pmatrix} 0 \\ 0 \\ g \end{pmatrix} = -\rho g \delta_{i3},$$

with g the gravitational accelleration. In addition to conservation of mass and momentum, conservation of internal energy must also be accounted for. This is done in the form of the energy or heat equation (again, see Bird *et al.* [4]):

$$\begin{aligned} \rho c_p\left(\frac{\partial T}{\partial t} + u_j \frac{\partial T}{\partial x_j}\right) &= -\frac{\partial q}{\partial x_j} - p\frac{\partial u_k}{\partial x_k} + \epsilon, \\ q &= -\lambda \frac{\partial T}{\partial x_j}, \\ \epsilon &= \frac{\mu}{2}\left(\frac{\partial u_i}{\partial x_j} + \frac{\partial u_j}{\partial x_i}\right)^2 - \frac{2}{3}\mu\left(\frac{\partial u_k}{\partial x_k}\right)^2, \end{aligned} \tag{2.3}$$

where c_p is heat capacity, T is temperature, and λ is thermal conductivity. Again the terms on the left-hand side represent time rate of change and convective transport, whereas the terms on the right-hand side account for contributions due to conduction, compression and viscous dissipation respectively. This investigation will only consider incompressible liquids, so the second term on the right-hand side drops out. Also, the Mach number Ma = u/c (with c the speed of sound in the medium), is very low for all cases. That means that pressure fluctuations and therefore the rate of viscous dissipation ϵ can also be neglected (Poinsot and Veynante [5]). The continuity, momentum balance, and heat equation together form the basis for describing the physical phenomena that are under investigation in this project.

2.1.2. THE OBERBECK-BOUSSINESQ APPROXIMATION

Fluid properties such as viscosity may vary throughout the system, mainly depending on temperature. However, if these variations remain sufficiently small, it is usually convenient to apply a combination of simplifications commonly referred to as the Oberbeck-Boussinesq (OB) approximation (see Oberbeck [6]). In general, this approximation consists of the assumptions:

- The density ρ is constant in every term except for the gravitational force term.
- The viscosity μ, heat capacity c_p and thermal conductivity λ of the fluid can be considered constant.
- The gravitational force term can be simplified by linearizing density as a function of temperature.

The first two assumptions lead to a simplified version of the balance equations:

$$\frac{\partial u_j}{\partial x_j} = 0, \tag{2.4}$$

$$\rho_0 \left(\frac{\partial u_i}{\partial t} + u_j \frac{\partial u_i}{\partial x_j} \right) = \frac{\partial p}{\partial x_i} + \mu \frac{\partial^2 u_i}{\partial x_j^2} - \rho g \delta_{i3}, \tag{2.5}$$

$$\frac{\partial T}{\partial t} + u_j \frac{\partial T}{\partial x_j} = \alpha \frac{\partial^2 T}{\partial x_j^2}, \tag{2.6}$$

with ρ_0 the mean density, and $\alpha = \lambda / \rho_0 c_p$ the thermal diffusivity, both of which are constant throughout the system. The third assumption can be implemented in the following form, to further simplify the momentum balance equation:

$$\begin{aligned} \rho &\approx \rho_0 [1 - \beta (T - T_0)], \\ \beta &= \frac{1}{\rho_0} \left. \frac{\partial \rho}{\partial T} \right|_{p=\text{constant}}, \end{aligned} \tag{2.7}$$

where β is the volumetric thermal expansion coefficient, and $T_0 = (T_b - T_t)/2$ is the mean temperature for which density attains its reference value ρ_0. Then the gravitational, or buoyancy term can be rewritten:

$$\rho_0 \left(\frac{\partial u_i}{\partial t} + u_j \frac{\partial u_i}{\partial x_j} \right) = -\frac{\partial p}{\partial x_i} + \mu \frac{\partial^2 u_i}{\partial x_j^2} - \rho_0 [1 - \beta (T - T_0)] g \delta_{i3}, \tag{2.8}$$

or, after some manipulation:

$$\frac{\partial u_i}{\partial t} + u_j \frac{\partial u_i}{\partial x_j} = -\frac{\partial}{\partial x_i} \left(\frac{p}{\rho_0} + g z \right) + \beta (T - T_0) g \delta_{i3} + \nu \frac{\partial^2 u_i}{\partial x_j^2}, \tag{2.9}$$

with $\nu = \mu / \rho_0$ the (constant) kinematic viscosity. This then, is the final form of the momentum equation with the full Boussinesq approximation. Again, the left-hand side represents time rate of change and convective transport. The right-hand side accounts for contributions by pressure gradients (corrected with a form of hydrostatic pressure), buoyancy, and viscous stress. Note that this form only applies to systems where fluid properties do not vary much, which is usually the case for situations where temperature differences are small. Gray and Giorgini [7] determined that variations in β, ν and α should not exceed 10% in order for the full OB approximation to be valid. This investigation mainly considers situations where this is not (entirely) the case, which we will refer to as Non-Oberbeck-Boussinesq (NOB). However, density fluctuations remain small ($< 2\%$) in all of the cases, so a partial OB approximation is allowed:

$$\frac{\partial u_j}{\partial x_j} = 0, \tag{2.10}$$

$$\frac{\partial u_i}{\partial t} + u_j \frac{\partial u_i}{\partial x_j} = -\frac{1}{\rho_0} \frac{\partial p}{\partial x_i} - \frac{\rho}{\rho_0} g \delta_{i3} + \frac{\partial}{\partial x_j} \left(\nu \frac{\partial u_i}{\partial x_j} \right), \tag{2.11}$$

$$\frac{\partial T}{\partial t} + u_j \frac{\partial T}{\partial x_j} = \frac{\partial}{\partial x_j} \left(\alpha \frac{\partial T}{\partial x_j} \right). \tag{2.12}$$

This version does not neglect the variations in ν and α, or linearize ρ, but does assume that density variations are only relevant in the buoyancy term. A simplification that is particularly useful when doing a statistical analysis using Reynolds decomposition, as will be shown in the following section. These equations are also discretized and implemented in the code for simulation.

2.1.3. REYNOLDS DECOMPOSITION

When analysing turbulent flow, a useful practise is to decompose output variables into a mean (time-averaged) part and fluctuating part, denoted by an overline and a prime:

$$\Phi = \bar{\Phi} + \Phi', \tag{2.13}$$

$$\bar{\Phi} = \frac{1}{T} \int_{t-T/2}^{t+T/2} \Phi \, dt, \tag{2.14}$$

with Φ the instantaneous value of the output variable of choice, and T the averaging time. The time-averaging operator obeys a number of general rules (see Nieuwstadt [8]), that will be useful in averaging the full equations with the decomposed variables later on. In theory, the averaging time must be infinite, but accurate results are generally obtained if the averaging time is chosen much larger than the time scale of turbulent fluctuations. For an OB-approximated situation, the variables that should be decomposed are the velocity components, pressure, and temperature. However, seeing as this investigation is primarily concerned with the effects of thermophysical property variations on the flow, temperature-induced fluctuations in these properties must also be taken into account:

$$\begin{aligned} u_i &= \bar{u}_i + u_i', \\ p &= \bar{p} + p', \\ T &= \bar{T} + T', \\ \rho &= \bar{\rho} + \rho', \\ \nu &= \bar{\nu} + \nu', \\ \alpha &= \bar{\alpha} + \alpha'. \end{aligned} \tag{2.15}$$

After substituting these decompositions into the governing equations, the full equations can be averaged in time according to the aforementioned rules. If one were to decompose and average after assuming constant ρ, μ, c_p and λ, one would obtain the standard Reynolds Averaged Navier-Stokes (RANS) equations for momentum. In this case, the derivation of the averaged equations must be done for the partially simplified versions 2.10, 2.11, and 2.12. This yields, after manipulation (see appendix A for a full derivation):

$$\frac{\partial \bar{u}_j}{\partial x_j} = 0, \tag{2.16}$$

$$\frac{\partial \bar{u}_i}{\partial t} + \bar{u}_j \frac{\partial \bar{u}_i}{\partial x_j} = -\frac{1}{\rho_0}\frac{\partial \bar{p}}{\partial x_i} - \frac{\bar{\rho}}{\rho_0} g \delta_{i3} + \frac{\partial}{\partial x_j}\left(\bar{\nu}\frac{\partial \bar{u}_i}{\partial x_j} + \overline{\nu' \frac{\partial u_i'}{\partial x_j}} - \overline{u_i' u_j'} \right), \tag{2.17}$$

$$\frac{\partial \bar{T}}{\partial t} + \bar{u}_j \frac{\partial \bar{T}}{\partial x_j} = \frac{\partial}{\partial x_j}\left(\bar{\alpha}\frac{\partial \bar{T}}{\partial x_j} + \overline{\alpha' \frac{\partial T'}{\partial x_j}} - \overline{u_j' T'} \right). \tag{2.18}$$

A number of terms involving fluctuating components have appeared. Two of these terms are well-known from turbulence literature: $\overline{u_i' u_j'}$ being the Reynolds stresses, and $\overline{u_j' T'}$ being the turbulent heat flux. The terms that involve ν' and α', but also the deviations of $\bar{\rho}$, $\bar{\nu}$ and $\bar{\alpha}$ from their OB-approximated counterparts are less well-known, and represent the direct influences of NOB effects. In this investigation, only statistically stationary situations are of interest, meaning that all time derivatives can be neglected from the averaged equations. That also implies that the other terms are expected to balance out. In this way, NOB effects can influence the mean velocity profile through the advective term and the viscous stress, but also turbulent aspects through the Reynolds stress and the turbulent heat flux. Finally, the turbulent kinetic energy (TKE) $e = \frac{1}{2}\overline{u_i'^2}$ is a measure of the local amount of total kinetic turbulence. Its obeys a balance equation, in which the production term follows from the shear stress (see Nieuwstadt [8]):

$$P = -\overline{u_i' u_j'}\frac{\partial \bar{u}_i}{\partial x_j}. \tag{2.19}$$

Therefore, NOB-related changes in the mean velocity field can indirectly affect the distribution of turbulent kinetic energy, and with it possibly also other turbulent quantities.

2.1.4. DIMENSIONLESS NUMBERS

As is the case for many applications in transport phenomena, it is convenient to derive a dimensionless version of the governing equations for RB convection. This is done by introducing characteristic parameters for the length scale (the distance between the hot and cold plate H), the velocity (α/H) and the temperature

difference between the bottom and top plates ($\Delta T \equiv T_b - T_t$). Then the dimensionless variables are:

$$\begin{aligned} x_i^* &\equiv x_i / H, \\ u_i^* &\equiv u_i H / \alpha, \\ t^* &\equiv t\alpha / H^2, \\ T^* &\equiv (T - T_0)/\Delta T, \\ p^* &\equiv p H^2 / (\rho_0 \alpha^2), \end{aligned} \tag{2.20}$$

which yields the following dimensionless form of equation 2.2:

$$\frac{1}{\mathrm{Pr}} \left[\frac{\partial u_i^*}{\partial t^*} + u_j^* \frac{\partial u_i^*}{\partial x_j^*} + \frac{\partial p^*}{\partial x_i^*} \right] = \frac{\partial^2 u_i^*}{\partial x_j^{*2}} + \mathrm{Ra} T. \tag{2.21}$$

Here Pr and Ra are the Prandtl and Rayleigh number, defined as:

$$\mathrm{Pr} = \frac{\nu}{\alpha}, \tag{2.22}$$

$$\mathrm{Ra} = \frac{g\beta\Delta T H^3}{\nu\alpha} = \frac{g\beta\Delta T H^3}{\nu^2} \frac{\nu}{\alpha} = \mathrm{Gr}\,\mathrm{Pr}. \tag{2.23}$$

The Prandtl number is a measure for the ratio of momentum diffusion to thermal diffusion in the fluid, and the Grashof number Gr is a measure for the ratio of buoyancy forces to viscous forces. That means that the Rayleigh number indicates the extent to which the driving buoyancy force prevails over the dampening effects of viscous and thermal diffusion, and determines the general flow characteristics. For this report, seeing as it deals with (strong) variations in ν, α and β, the case-specific Prandtl and Rayleigh numbers are chosen to be defined at the reference temperature T_0. Analogously, the Nusselt number can be derived from the heat equation and is defined as (see Bird *et al.* [4]):

$$\mathrm{Nu} = \frac{qH}{\lambda \Delta T}, \tag{2.24}$$

where q is the convective heat flux through a boundary of choice. The Nusselt number is then a measure for the ratio of convective to conductive heat transfer normal to that boundary. For RB convection however, it is most often used as a measure of the total dimensionless heat transfer through the system. It is then calculated as a surface integral average over the top or bottom wall, of the dimensionless conductive heat flux in the vertical direction:

$$\overline{\mathrm{Nu}} = \iint_S \frac{\partial T^*}{\partial z^*} dx^* dy^*. \tag{2.25}$$

2.2. RELATED RESEARCH

Free convection has been a widely studied subject in literature, since Bénard [9] performed the first quantitative experiments in this field (see for example, Strutt Baron Rayleigh [10]). As mentioned before, it is important in many industrial applications and reference problems are therefore of great interest. With the increase of computational power, computational fluid dynamics (CFD) codes have become a useful tool in that regard, and the first numerical simulations were conducted as early as 1976. This section will provide the reader with a short overview of research that is related to, and relevant to the understanding of this investigation.

2.2.1. BOUNDARY LAYERS AND LARGE SCALE CIRCULATION

Most research in turbulent RB convection concentrates on understanding the large scale flow dynamics. These flow structures involve thermal and viscous boundary layers developing at the walls. It should be noted here that, unlike in other turbulence topics, there is no formal definition of a boundary layer in the context of RB convection. Instead, these boundary layers are most commonly defined based on the spatial derivatives of velocity and temperature gradient at, and normal to the wall. For now, only a qualitative definition in terms of those derivatives will suffice:

$$\delta_t \propto \left| \frac{\partial T}{\partial x_k} \right|^{-1}, \tag{2.26}$$

$$\delta_v \propto \left| \frac{\partial u_i}{\partial x_k} \right|^{-1}, \tag{2.27}$$

where x_k is chosen normal to the wall, with δ_t the thermal boundary layer thickness and δ_v the viscous boundary layer thickness (see Ahlers *et al.* [11] for a more elaborate discussion). Thermal plumes erupt from the thermal boundary layers at the top and bottom plates (see figure 2.2(a)). In this way, the thermal boundary layers discharge their heat, after which they recharge from the conducting plates. The thermal plumes drive the mean flow, which takes the form of a roll structure. In turn, the mean flow stimulates the formation of plumes from the boundary layers. The developed roll structure is commonly referred to as the large scale circulation (LSC), and it is constantly accellerated by the thermal plumes. In that sense, it is not necessarily stable, but it's time averaged form takes on a symmetrical shape (see figure 2.2(b)). In a roll structure that consists of multiple rolls, each individual roll is known as an RB cell.

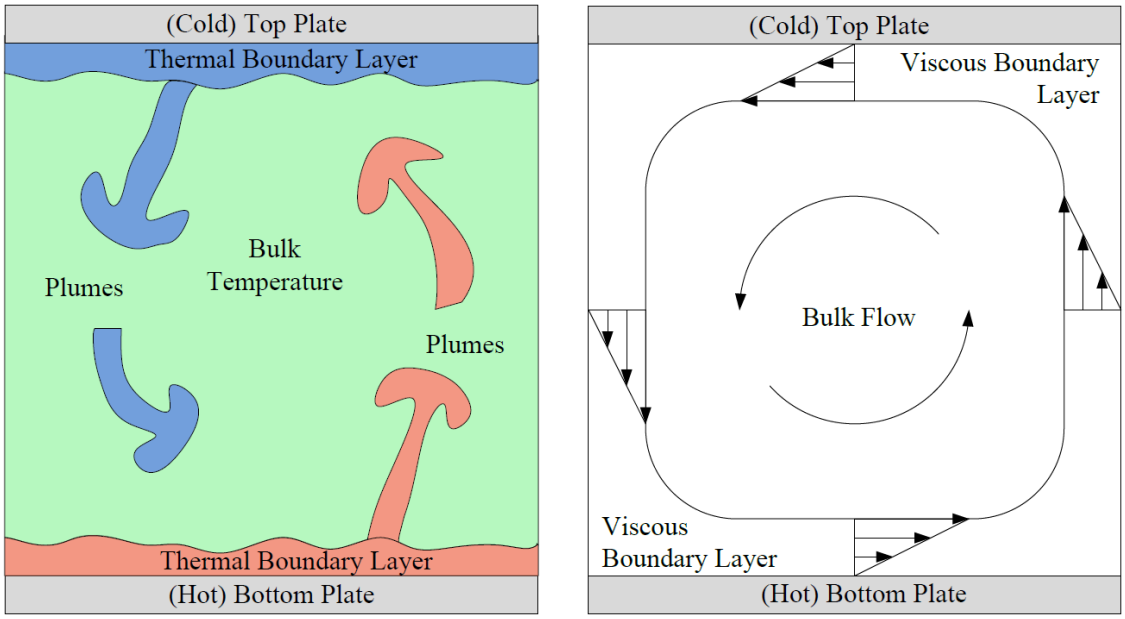

(a) Thermal plumes and boundary layers

(b) Large scale circulation

Figure 2.2: Schematic example of an RB cell, taken from Ahlers *et al.* [12].

2.2.2. GROSSMANN-LOHSE THEORY

Grossmann and Lohse [13] developed a theory relating $\mathrm{Nu} = f(\mathrm{Ra}, \mathrm{Pr})$ scaling relations to the contributions to energy dissipation. They compared contributions of viscous and thermal dissipation (ϵ and η) in both the boundary layers and the bulk flow, and by doing so obtained four regimes in the Ra-Pr space (see figure 2.3 and table 2.1). Each regime represents different scaling relations, relative boundary layer size and contributions to thermal and viscous dissipation. This is relevant to the present study, because viscosity variations in particular are known to show important interaction with the boundary layer structure.

Regime	BL size	ϵ dominated by	η dominated by
I_l	$\delta_t < \delta_v$	BL	BL
I_u	$\delta_t > \delta_v$	„	„
II_l	$\delta_t < \delta_v$	BL	bulk
(II_u)	$\delta_t > \delta_v$	„	„
III_l	$\delta_t < \delta_v$	bulk	BL
III_u	$\delta_t > \delta_v$	„	„
IV_l	$\delta_t < \delta_v$	bulk	bulk
IV_u	$\delta_t > \delta_v$	„	„

Table 2.1: Four scaling regimes in Ra-Pr-space, from Grossmann and Lohse [13].

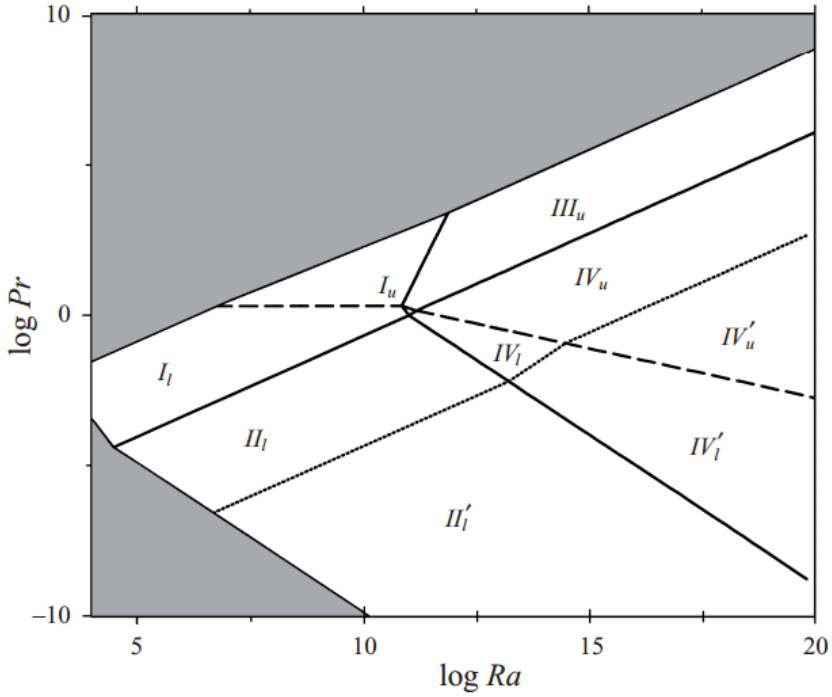

Figure 2.3: Phase diagram showing the scaling regimes in Ra-Pr space, from Grossmann and Lohse [13].

2.2.3. THE CUBICAL CAVITY

One of the aforementioned reference problems in RB convection is the cubical cavity heated from below, mainly because it is a convenient geometry to study the transition to turbulence (see Busse [14]). Pallares *et al.* [15] conducted a series of experimental and numerical studies on both laminar and turbulent cases, focussed on documenting and understanding the LSC structures in such a cavity. They reported experimentally observed stable roll structures (single and toroidal) for different laminar Rayleigh numbers. Interestingly, roll structures that formed when the Rayleigh number was increased, sometimes remained stable after the Rayleigh number was decreased again. Subsequential studies by the same group (Pallares *et al.* [16] and Valencia *et al.* [3]), reported similar findings for both the laminar and turbulent regime.

2.2.4. NON-OBERBECK-BOUSSINESQ EFFECTS

Valencia *et al.* [17] also conducted a computational study on the influence of NOB-properties on turbulent and laminar flow in a cubical cavity heated from below. A comparison was made between simulations of an NOB case by four solvers calculating different NOB contributions, in order to isolate these influences. They concluded that even though the property variations of 62% for β and 40% for ν well exceeded the aforementioned 10% threshold for the OB approximation, the flow topologies were not significantly affected. Fow low Rayleigh numbers (1×10^4 and 5×10^4), they found an increase and decrease by 5% of the maximum velocity at the hot and cold plate, respectively. However, this resulted in an increase of the Nusselt number by only 3% and 4.5%. For turbulent flows at a Rayleigh number of 10^7, the differences were even smaller: 1.3% difference in velocity and 1% increase in Nusselt number. Their reasoning was that the variations in thermophysical properties were on average mainly restricted to the thin thermal boundary layers, and that large scale dynamics and heat transfer were therefore largely unaffected.
Ahlers *et al.* [11, 18] investigated NOB effects in strongly turbulent flow both experimentally and computationally. They too, found that the influences of NOB effects on for example the Nusselt number are negligible, even for property variations of factor 2 or more. Their prediction was that, although the boundary layer structure becomes vertically asymmetrical for NOB situations due to viscosity variations, the total vertical boundary layer thickness remains the same and therefore Nu and Re are largely unaffected. Furthermore, they found that the thermal boundary layers remain laminar for moderate Rayleigh numbers, even though the bulk flow is turbulent. At higher Rayleigh numbers the boundary layers themselves become turbulent as well. Their prediction was that the turbulent boundary layers do not influence the Nusselt number, and therefore the influence of NOB effects decreases as the Rayleigh number increases.

3

NUMERICAL METHOD

This chapter provides an explanation of the numerical method and the reasoning behind it, along with an overview of the different case parameters.

3.1. PROBLEM DESCRIPTION

As was mentioned in the previous chapter, the cases simulated in this investigation feature a rigid cubical cavity, with a constant temperature condition at the top and bottom walls. The temperature at the sidewalls T_s can be defined by either a linear profile in the vertical direction (conducting), or a zero gradient in the surface normal direction (adiabatic). Different sizes of cavities are used, depending on the desired Rayleigh numbers and temperature differences. Table 3.1 presents an overview of the defining parameters per case, including the maximum variation for each relevant thermophysical fluid property.

Parameter	Case 1	Case 2	Case 3	Case 4	Case 5	Case 6	Case 7
Fluid	silicon oil	silicon oil	water	water	water	methanol	water
OB/NOB	OB	OB	OB*	NOB	NOB	OB*	NOB
Ra	10^4	4×10^4	10^7	10^4	10^7	6.74×10^8	6.91×10^8
Pr	130	130	6.04	6.04	6.04	7.23	4.08
H (m)	0.05	0.05	0.05	0.0031	0.0313	0.077	0.077
T_s	adiabatic	adiabatic	conducting	conducting	conducting	adiabatic	adiabatic
ΔT (K)	0.37	1.5	4.07	17.1	16.6	9.6	40
$\Delta\rho$ (%)	-	-	0.12	0.45	0.43	1.04	1.53
$\Delta\beta$ (%)	-	-	15.3	65.1	63.3	49.1	87.7
$\Delta\mu$ (%)	-	-	10.6	43.7	42.4	14.4	87.9
$\Delta\lambda$ (%)	-	-	1.32	5.67	5.51	3.16	7.14
Δc_p (%)	-	-	0.04	0.20	0.19	0.17	0.17

Table 3.1: Specifications of the simulated cases.

The first five cases were conducted in the order described in the project goals. This procedure ensured a structured and failsafe approach of the project goals mentioned in section 1.3. Cases 1-3 are primarily intended for comparison with reference data from Pallares *et al.* [15, 16]. Cases 4 and 5 are reproductions of simulations by Valencia *et al.* [17], and cases 6 and 7 are an attempt to reproduce in-house experimental data by Valentina Valori. Discussion of the results will be by means of comparison of case 3 with case 5, and case 6 with case 7. The characteristics of cases 3-7 have the following notable implications for the solver:

- The solver must be able to resolve all scales of turbulence.
- The solver must be able to account for temperature-dependent thermophysical properties.

It is mainly the combination of these requirements that is an important restriction in selecting the solver, as will be explained in the following section. Furthermore, from the property data it is evident that the variations in ρ remain relatively small in every simulation. Therefore, equations 2.10, 2.11, and 2.12 can be used for implementation in the code.

3.2. NUMERICAL METHOD

The OpenFOAM software package offers a wide variety of numerical methods and customization options. This section gives a brief overview of the considerations that were taken into account when determining the most appropriate method for this investigation.

3.2.1. SOLVER

There are multiple approaches available to solve the continuity equation, the momentum balance equations, and the heat transfer equation numerically. Each approach has its own advantages and disadvantages and the characteristics of the problem to be solved will determine which is the most suited approach for the job (if there is one). This research aims at investigating the influence that variations in temperature dependent properties have on the flow, a case that is particularly difficult to model at the sub-grid scale. Therefore, all simulations are performed using direct numerical simulation (DNS). DNS is the most accurate computational method for predicting turbulent flows, because it fully resolves all length scales in the flow (as opposed to using a turbulence model). This results in an increase in required mesh resolution at the cost of processing time. The solver that is used is an adaptation of the standard supplied buoyantBoussinesqPimpleFoam solver. The original code uses a combination of the PISO and SIMPLE algorithms (see Hanjalić *et al.* [19]), and it is modified to allow for the manual implementation of thermophysical property variation. A MATLAB script is used to fit property data with a polynomial function of temperature, according to:

$$\Phi(T) = c_0 + c_1 T + c_2 T^2 + c_3 T^3, \tag{3.1}$$

with $\Phi(T)$ the instantaneous local property value, and c_i the i-th coefficient for that property. An example of such a fit for viscosity is given in figure 3.1. See appendix B for an overview of the thermophysical property data and the polynomial fits.

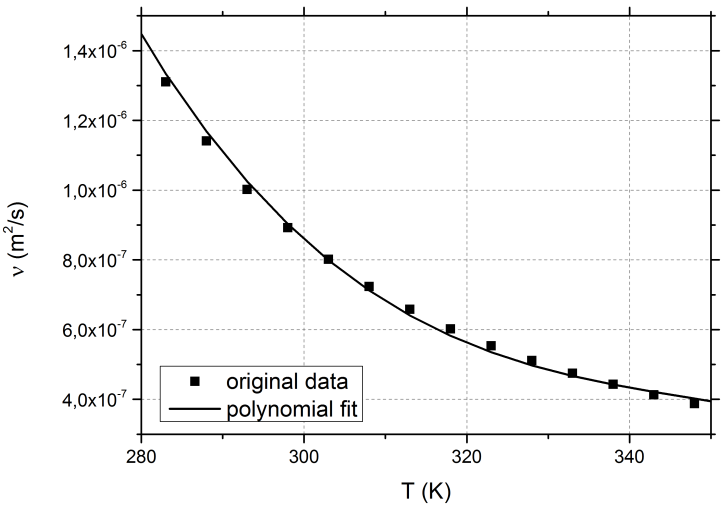

Figure 3.1: Original data and polynomial fit for the kinematic viscosity of water.

3.2.2. DISCRETIZATION SCHEMES

In turbulent computational fluid dynamics, both the spatial and temporal domain must be discretized. For the spatial domain, three standard discretization methods are available, being the finite element method (FEM), the finite difference method (FDM), and the finite volume method (FVM). The method applied in this investigation is the finite volume method. When using the finite volume method, the spatial domain is split up into cells, and the conserved variables are calculated for each cell. Volume integrals in partial differential equations can be converted to surface integrals over the cell faces by application of Gauss's theorem, resulting in a natural way of conserving quantities. The central differencing scheme (CDS) is used to calculate central and face node values. It is easily implemented numerically, because it uses linear interpolation between

two cell face nodes to obtain an approximation for the central node value, and it is therefore second order accurate. Because the scheme is unbounded, it is not unconditionally stable (Hanjalić *et al.* [19]).
Temporal discretization (or time integration) methods can generally be divided in two categories: explicit and implicit schemes. Explicit schemes solve explicitly for the value of a variable at a new time instant; it is expressed as a function of known values at an earlier time instant. On the contrary, implicit schemes solve for unknown values at a new time instant as a function of both known current and unknown new values. For this investigation, a first order bounded implicit scheme is used. The OpenFOAM solver is able to automatically adjust the time step to a suitable value, through the Courant-Friedrichs-Lewy condition:

$$C = \Delta t \left(\frac{u_i}{\Delta x} + \frac{u_j}{\Delta y} + \frac{u_k}{\Delta z} \right) \leq C_{\max}. \tag{3.2}$$

Here C is the Courant number, $C_{\max}$ its maximum attainable value, and $\Delta x, \Delta y, \Delta z$ the local grid spacing in all three directions. The Courant number expresses the ratio between the distance travelled by a fluid parcel in a single time step, and the maximum travelled distance that the grid resolution can account for. Generally speaking, the Courant number cannot exceed a maximum value of 1, but in this research a maximum of 0.5 is used. The solver will automatically adjust the time-step so that this maximum is not exceeded.

3.2.3. MESH RESOLUTION

To accurately and correctly simulate a turbulent flow, an appropriate mesh resolution is required. This resolution can be determined empirically by trial and error, but it is convenient to predict the appropriate resolution beforehand. Grötzbach [20] established a method for calculating appropriate mesh resolutions in the case of turbulent Rayleigh-Bénard convection. For this specific research, which does not involve a cyclic geometry, two requirements must be taken into consideration:

- The grid spacing near the walls must be sufficiently small to resolve the temperature gradients in the thermal boundary layers.
- The average grid spacing must be sufficiently small to resolve the smallest turbulent fluctuations.

To satisfy the first requirement the thickness of the thermal boundary layer must be calculated:

$$\delta_t = \frac{1}{2\mathrm{Nu}}, \tag{3.3}$$

$$\mathrm{Nu} \approx 0.19\mathrm{Ra}^{0.282}, \tag{3.4}$$

According to Grötzbach, it is advisable to place at least 2 nodes in the thermal boundary layer for laminar flows, and 3 for turbulent flows. Calculating the second requirement is a bit more complicated. Depending on the Prandtl number, the smallest turbulent fluctuations can be either momentum fluctuations or thermal fluctuations. In the first case the smallest length scale is the Kolmogorov scale η, and in the second it is the Batchelor scale η_T. The minimum average dimensionless grid spacing d^* can be calculated as follows:

$$d^* \leq 5.13 \left(\frac{\mathrm{Pr}^2}{\mathrm{Ra\,Nu}} \right)^{1/4} \qquad \text{for} \qquad \mathrm{Pr} \leq 1, \tag{3.5a}$$

$$d^* \leq 3.45 \left(\frac{1}{\mathrm{Ra\,Pr\,Nu}} \right)^{1/4} \qquad \text{for} \qquad \mathrm{Pr} \geq 1. \tag{3.5b}$$

All of the cases in this investigation simulate the thermophysical properties of fluids with a Prandtl number larger than 1. Also, as mentioned before, the Rayleigh, Prandtl and Nusselt numbers are chosen to be defined at the reference temperature T_0, to accurately represent the turbulent behaviour in the bulk flow. In the thermal boundary layers the Prandtl number can be higher. This consideration is taken into account by using grid refinement near the walls, which is also necessary to satisfy the first requirement provided by Grötzbach [20]. Computing these requirements for the different parameters of each individual simulation will result in a prediction for the minimum number of cells in each direction $N_{\min} = 1/h$ (see table 3.2). Because of the limited available CPU power, the number of cells in each direction $N = N_x = N_y = N_z$ was limited to a maximum of 70, with refinement near the walls (see figure 3.2). This means that the code is not able to resolve a large portion of the turbulent length scales for cases 6 and 7, which should be taken into account for statements with respect to turbulent quantities in those two cases.

Parameter	Case 1	Case 2	Case 3	Case 4	Case 5	Case 6	Case 7
Ra	10^4	4×10^4	10^7	10^4	10^7	6.74×10^8	6.91×10^8
Pr	130	130	6.04	6.04	6.04	7.23	4.08
δ (%)	19.6	13.3	2.79	19.6	2.79	0.85	0.85
N_{min}	-	-	53	-	53	212	185
N	40	40	70	40	70	70	70

Table 3.2: Calculated mesh resolution requirements for the cases in the turbulent regime.

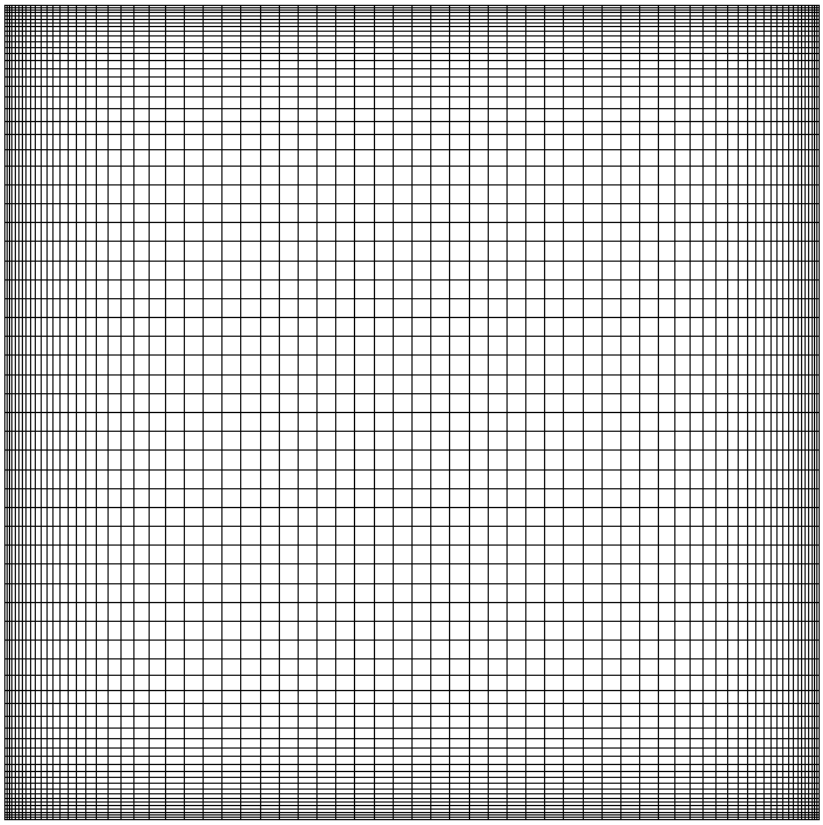

Figure 3.2: Frontal view of the simulation mesh with $N_{xyz} = 70$.

4

VALIDATION

In order to verify the validity of the code used in this investigation in predicting RB convection, a number of reference cases was selected for comparison from the available literature by Pallares *et al.* [15] and Valencia *et al.* [3, 17]. This chapter will present the reader with the compared data in chronological order. All dimensionless quantities are defined as described in section 2.1.4.

4.1. OBERBECK-BOUSSINESQ

As was mentioned in the previous chapter, some OB cases were conducted before the NOB cases. That way, an OB version of the solver could be validated and subsequently modified to account for property variations. The specifications of the OB cases are given once more in table 4.1. Strictly speaking, case 3 can not be considered fully OB, because the variations in β and ν exceed the allowed 10%. However, Pallares et al. showed in their report that the results by an OB solver are still accurate enough to consider it appropriate for this case.

Parameter	Case 1	Case 2	Case 3
Fluid	silicon oil	silicon oil	water
OB/NOB	OB	OB	OB*
Ra	10^4	4×10^4	10^7
Pr	130	130	6.04
H (m)	0.05	0.05	0.05
T_s	adiabatic	adiabatic	conducting
ΔT (K)	0.37	1.5	4.07
$\Delta\rho$ (%)	-	-	0.12
$\Delta\beta$ (%)	-	-	15.3
$\Delta\mu$ (%)	-	-	10.6
$\Delta\lambda$ (%)	-	-	1.32
Δc_p (%)	-	-	0.04

Table 4.1: Specifications of the OB validation cases.

4.1.1. LAMINAR REGIME

The first two reference cases (see Pallares *et al.* [15]) were chosen in the laminar regime, and therefore a steady-state algorithm was used. These cases considered RB convection in silicone oil in a cubical cavity, both experimentally and computationally. A comparison was made by plotting dimensionless velocity components taken at the horizontal and vertical centerlines (see figure 4.1). From this figure it is clear that there are differences with the experimental results, for which various explanations are possible. However, the agreement with the numerical reference data is good, and so the code can be considered valid in predicting OB laminar flow.

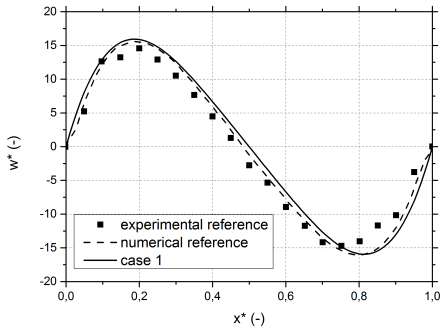

(a) Vertical velocity component at the line $y^* = 0.5$, $z^* = 0.5$ for Ra = 10^4.

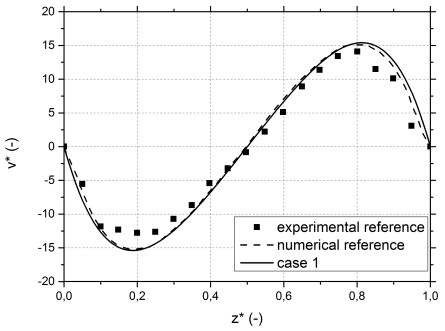

(b) Horizontal velocity component at the line $x^* = 0.5$, $y^* = 0.5$ for Ra = 10^4.

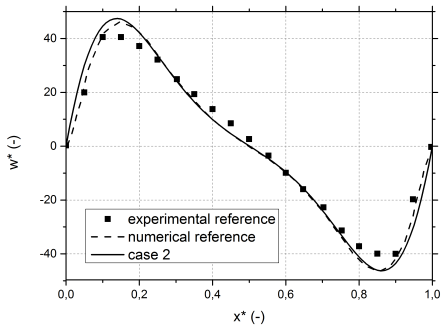

(c) Vertical velocity component at the line $y^* = 0.5$, $z^* = 0.5$ for Ra = 4×10^4.

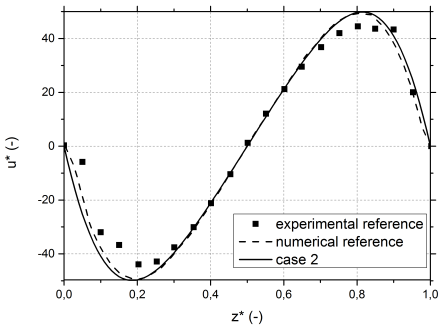

(d) Horizontal velocity component at the line $x^* = 0.5$, $y^* = 0.5$ for Ra = 4×10^4.

Figure 4.1: Dimensionless velocity component comparison at the centerlines for two laminar reference cases from Pallares *et al.* [15]

4.1.2. TURBULENT REGIME

The second part of the OB validation was conducted by comparison with a case in the turbulent regime, by Valencia *et al.* [3]. This means that a time-dependent solving algorithm was used, and that the presented results are therefore time-integrated quantities (for an integration time of $t = 2000$ s of simulated time after stabilization). The case is a numerical study of RB convection in water in a cubical cavity. The comparison was made by plotting the time-averaged vertical velocity component near the bottom wall (see figure 4.2). The differences are small enough to consider the code valid in predicting OB turbulent flow.

4.2. NON-OBERBECK-BOUSSINESQ

For the following cases, the solver was modified to account for property variations. The specifications of the NOB cases are given once more in table 4.2. Initially, the intention was to validate the code by comparing cases 4 and 5 to reference simulation data by Valencia *et al.* [17]. Since the differences were too large for the code to be considered validated, a comparison with in-house experimental data by Valentina Valori for case 6 is also presented. Once again, the grid resolution is insufficient to resolve all turbulent length scales in case 6, which is why the cases by Valencia *et al.* [3] were initially preferred for comparison.

4.2.1. LAMINAR REGIME

As was mentioned in chapter 2, Valencia *et al.* [17] devoted a computational study to predicting RB convection with strong NOB effects. Cases 4 and 5 were conducted in an attempt to replicate their data, starting with case 4 for laminar flow. A comparison was made by plotting instantaneous dimensionless velocity components (see figure 4.3). From the plots it is evident that there is little to no agreement between the two simulations. The differences are so large that they cannot be attributed to for example, minor numerical errors. In other words, the code can not be considered valid in predicting NOB laminar flow at this point.

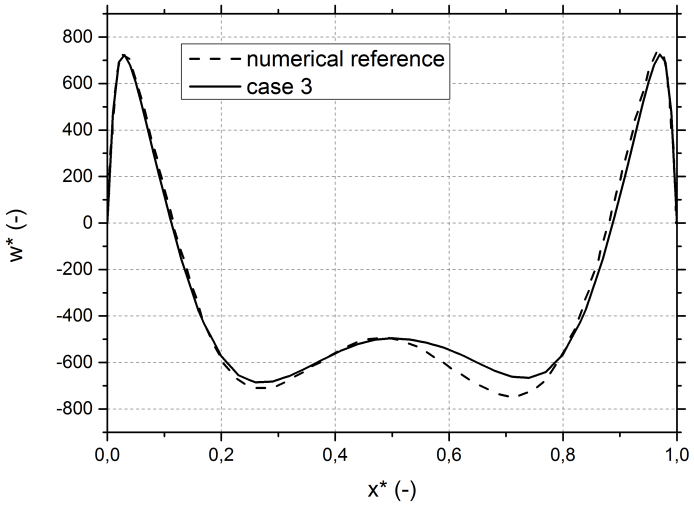

Figure 4.2: Dimensionless time-averaged vertical velocity component comparison for a turbulent reference case from Valencia et al. at the line $x^* = 0.5$, $z^* = 0.0222$ for Ra = 10^7.

Parameter	Case 4	Case 5	Case 7
Fluid	water	water	water
OB/NOB	NOB	NOB	NOB
Ra	10^4	10^7	6.91×10^8
Pr	6.04	6.04	4.08
H (m)	0.0031	0.0313	0.077
T_s	conducting	conducting	adiabatic
ΔT (K)	17.1	16.6	40
$\Delta\rho$ (%)	0.45	0.43	1.53
$\Delta\beta$ (%)	65.1	63.3	87.7
$\Delta\mu$ (%)	43.7	42.4	87.9
$\Delta\lambda$ (%)	5.67	5.51	7.14
Δc_p (%)	0.20	0.19	0.17

Table 4.2: Specifications of the NOB validation cases.

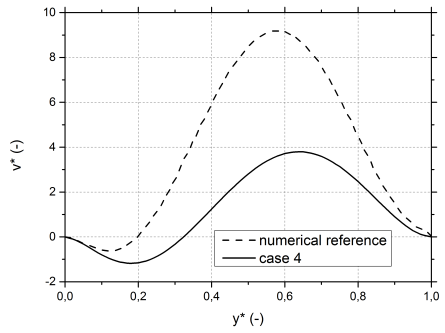

(a) Horizontal velocity component at the line $x^* = 0.5$, $z^* = 0.064$ for Ra = 10^4.

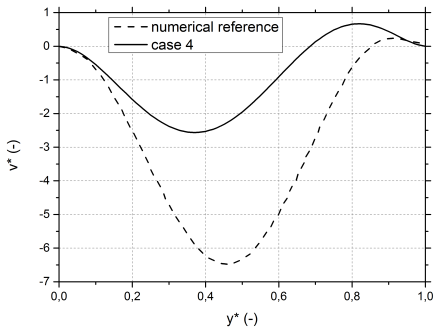

(b) Horizontal velocity component at the line $x^* = 0.5$, $z^* = 0.94$ for Ra = 10^4.

Figure 4.3: Dimensionless velocity component comparison for an NOB laminar reference case from Valencia *et al.* [17]

4.2.2. TURBULENT REGIME

Case 5 was conducted for comparison with the NOB case at Ra = 10^7 from the same article [17]. Contrary to the previous cases, there were no velocity profiles available, only time-averaged data at a specific location. Unfortunately, the agreement between the local simulation results and the reference data was once again insufficient. On the other hand, Valencia *et al.* [17] reported data for this one case, conducted by four different solvers: one OB solver, one NOB solver, one with only variable β, and one with only variable ν and α. They found no significant differences between the results generated using these solvers. For this investigation, the same four methods were applied, yielding similarly small differences. One could therefore argue that the dimensionless velocity field in a simulation at Ra = 10^7 should not be significantly different for either an OB or NOB case, respectively. This indeed appears to be the case when a comparison is made between cases 3 and 5, along with the reference data for case 3 from Valencia *et al.* [3] (see figure 4.4).

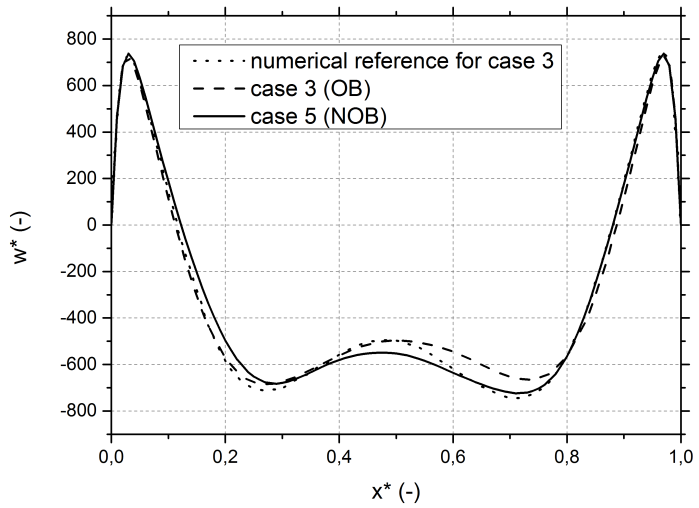

Figure 4.4: Dimensionless time-averaged vertical velocity component comparison between an OB and an NOB case at the line $x^* = 0.5$, $z^* = 0.0222$ for Ra = 10^7.

In order to still establish the trustworthiness of the code in predicting turbulent NOB flow, a comparison was made between case 7 and in-house experimental data for the same parameters by Valentina Valori. Velocity profiles at the horizontal and vertical centerlines are shown in figure 4.5, followed by contour plots of the velocity magnitudes in the y-z centerplane. It should be noted that, as was noted in chapter 3, the resolution of this case did not conform to the theoretical requirement. The available computational power did not allow for a higher resolution, given the available time in this investigation. That being said, the simulated and experimental data appear to agree quite well. In addition, the agreement improved as the resolution was increased. Therefore, the code can be considered valid in predicting NOB flow.

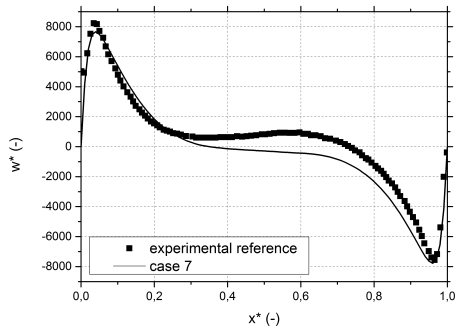

(a) Vertical velocity component at the horizontal centerline for Ra = 6.91×10^8.

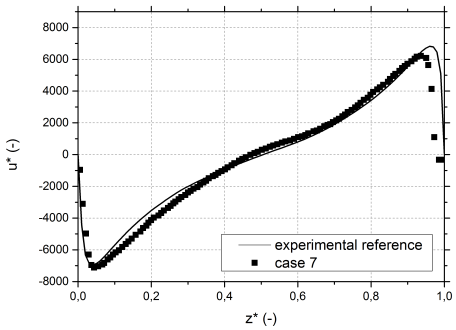

(b) Horizotal velocity component at the vertical centerline for Ra = 6.91×10^8.

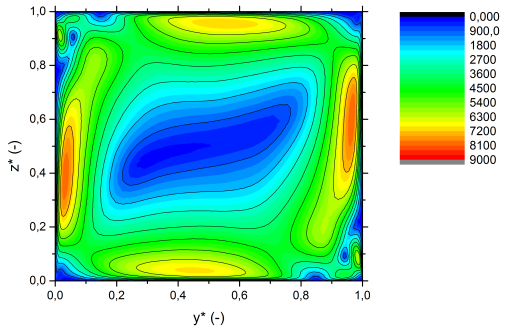

(c) Simulated velocity magnitude in the y-z centerplane for Ra = 6.91×10^8.

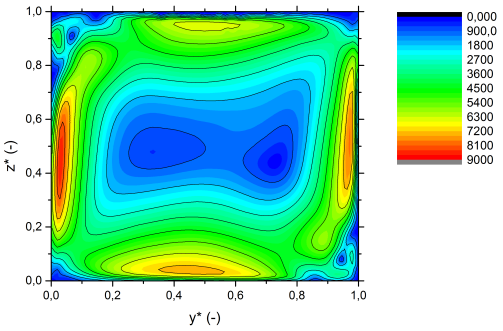

(d) Experimental velocity magnitude in the y-z centerplane for Ra = 6.91×10^8.

Figure 4.5: Dimensionless velocity component and magnitude comparison with data from a turbulent case by Valentina Valori. N.B.: the velocity magnitudes are in this case computed from only the velocities in the y-z centerplane: $|u^*| = \sqrt{v^{*2} + w^{*2}}$.

5

RESULTS AND DISCUSSION

This chapter will provide the reader with an overview and a discussion of the investigation results. OB and NOB flows are compared based on characteristics of property variations, followed by fluid motion and heat transfer. A term by term analysis of the governing equations is done for the first two cases, including a discussion of (changes in) turbulent characteristics of the flow. Again, all dimensionless quantities are defined as described in section 2.1.4.

5.1. CASE 3 VERSUS CASE 5

The first comparison is made between cases 3 (OB) and 5 (NOB), of which the relevant parameters are given once more in table 5.1. Throughout the remainder of this section, Δ is used to denote the changes of a dimensionless quantity in case 3 towards its counterpart in case 5, e.g. $\Delta\Phi^* = \Phi^*_5 - \Phi^*_3$.

Parameter	Case 3	Case 5
Fluid	water	water
OB/NOB	OB*	NOB
Ra	10^7	10^7
Pr	6.04	6.04
H (m)	0.05	0.0313
T_s	conducting	conducting
ΔT (K)	4.07	16.6
$\Delta\rho$ (%)	0.12	0.43
$\Delta\beta$ (%)	15.3	63.3
$\Delta\mu$ (%)	10.6	42.4
$\Delta\lambda$ (%)	1.32	5.51
Δc_p (%)	0.04	0.19

Table 5.1: Specifications of cases 3 and 5.

5.1.1. DISTRIBUTION OF PROPERTY VARIATIONS

In order to predict the local impact of thermophysical property variations, their spatial distributions are studied. As is evident from table 5.1, the most significant variations are seen in thermal expansivity and (dynamic) viscosity. As was explained in section 1.3, this investigation is primarily concerned with the impact of significant variations in viscosity. Figure 5.1 shows the normalized (kinematic) viscosity $\nu^* = \nu/\nu_0$ throughout the y-z centerplane for case 5. The spatial distribution of viscosity changes is as expected, based on the literature by Ahlers *et al.* [11] and Valencia *et al.* [17]: the strongest deviations (±20%) are, on average, confined to thin thermal boundary layers at the top and bottom walls, that extend along the sidewalls because of the linear temperature profile on the boundary. However, the instantaneous profile illustrates that property changes can be induced in the bulk on an instantaneous level, by thermal plumes erupting from the boundary layer. The instantaneous variations in the bulk of the right-hand sided plot are of the order of ±5%, and serve as a

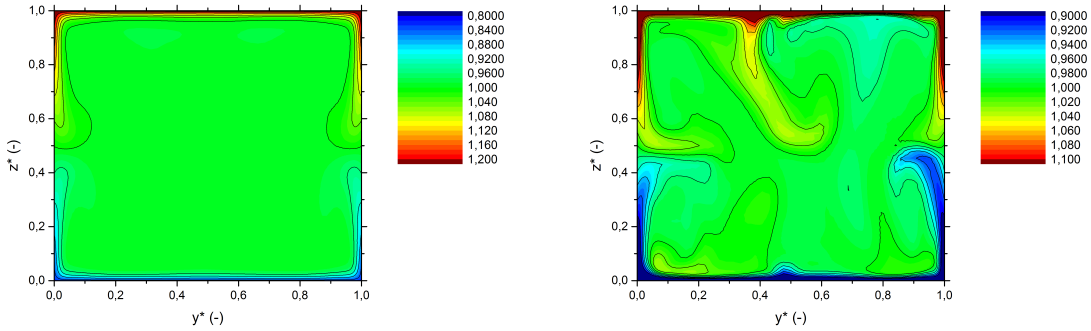

(a) Time-averaged distribution.

(b) Instantaneous distribution.

Figure 5.1: Normalized viscosity in the plane $x = 0.5$ for case 5.

good estimate for the local maxima and minima. Seeing as instantaneous viscosity variations are therefore not likely to exceed the 10% limit (Gray and Giorgini [7]) by a significant margin, they do not contribute much to the NOB effects on the mean flow. The following section will discuss the effects of the property changes on fluid motion.

5.1.2. EFFECTS ON FLUID MOTION

Figure 5.2 shows the velocity magnitude in the horizontal and vertical centerplanes for case 5.

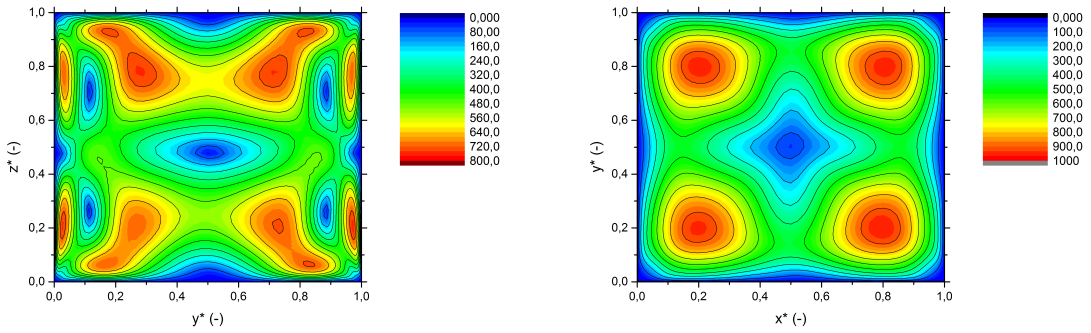

(a) Velocity magnitude in the y-z centerplane.

(b) Velocity magnitude in the x-y centerplane.

Figure 5.2: Dimensionless velocity magnitude in the plane $x = 0.5$ and the plane $z = 0.5$ for case 5.

It is evident that the flow geometry is symmetrical in both the x and y direction, with the x-z and y-z centerplanes being the planes of symmetry. The flow is also two-fold symmetrical with respect to rotation around the z-axis. All of these characteristics apply to both cases. Therefore, it is convenient to look at variations throughout the y-z centerplane, as they are analogous to variations in the x-z centerplane by rotational symmetry. In addition, it is not useful to investigate the momentum equation for u at the y-z centerplane, because there is no time-averaged fluid motion in the x direction in that plane and all components of the equation are therefore zero. Further investigation shows that the flow structure consists of an upper and a lower toroidal roll, as was explained by Valencia *et al.* [3]. A closer look at the velocity magnitude differences reveals that there is a complicated pattern of changes towards case 5. In order to get a qualitative and quantitative idea of these changes, changes in v^* and w^* are shown in figure 5.3.

It appears that the horizontal velocity magnitude in case 5 is approximately 5% higher at the bottom plate, and approximately 5% lower at the top plate, when compared to the corresponding local velocity in case 3. More significant however, are the changes in velocity near the vertical center. The NOB effects induce an upward flux in the region around the center of the cavity in case 5, combined with a downward flux through the vertical center near the sidewalls. These changes are accompanied by horizontal flow towards the center

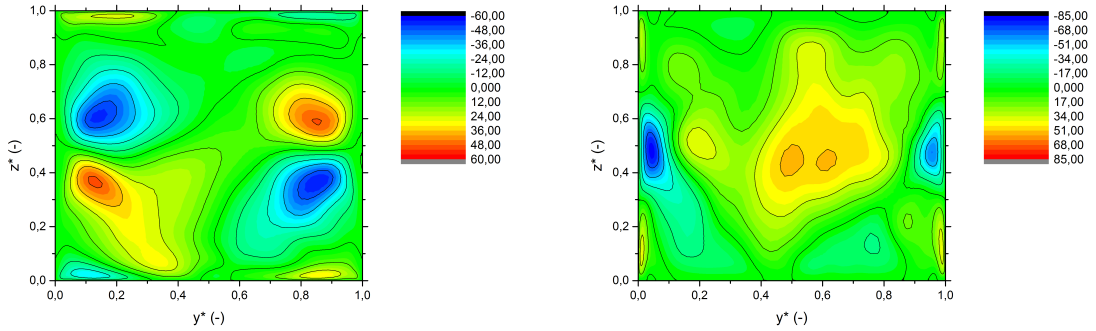

(a) Changes Δ in v^*.

(b) Changes Δ in w^*.

Figure 5.3: Changes in dimensionless velocity components in the plane $x^* = 0.5$.

just below the plane $z^* = 0.5$, and an approximately equal but opposite flow on the opposing side of that plane. The induced differences near the vertical center are all of the order of 10% of the highest velocities, and seem to add up to a third toroidal roll being formed around the center of the cavity. To further illustrate these differences, velocity profiles are shown in figure 5.4.

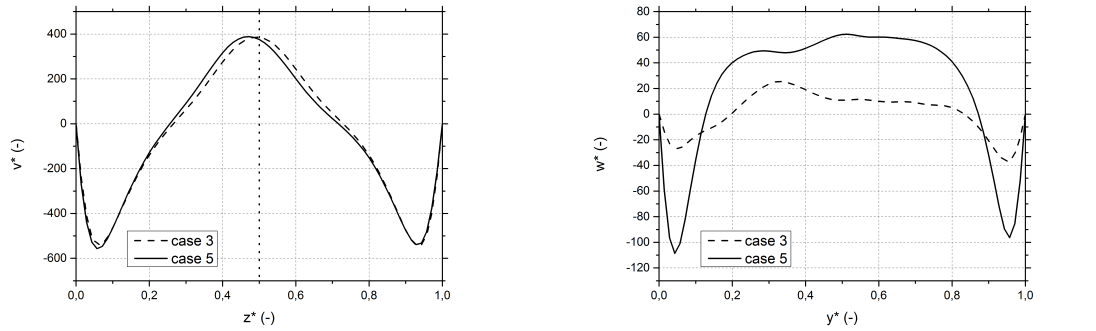

(a) Velocity component v^* on the line $x^* = 0.5$, $y^* = 0.1$.

(b) Velocity component w^* on the line $x^* = 0.5$, $z^* = 0.5$.

Figure 5.4: Dimensionless velocity components for cases 3 and 5.

The profile of v^* in case 5 is shifted in the vertical direction: the maximum is displaced by a nondimensional distance of 0.03 towards the bottom plate. This makes it asymmetrical with respect to the x-y centerplane (indicated by the dotted line), whereas the OB profile is close to symmetrical. The vertical velocity profile shows the most significant changes: the average upward velocity in the center and the downward velocity near the sidewalls are increased by approximately 400%. It should be noted here, that the OB approximation for this specific flow structure would require by symmetry that there is no velocity component normal to the vertical midplane. Clearly, case 3 does not conform to this symmetry and can not be considered a perfect example of an OB case. In addition, the velocity profiles at $z^* = 0.5$ are not perfectly symmetrical in the horizontal directions, which must be caused by insufficient averaging. However, these unintended asymmetrical aspects are small relative to the NOB-related changes of the flow, and therefore a qualitative and quantitative comparison is still useful. As was mentioned in section 2.2.4, NOB-related symmetry breaking in the vertical direction was also observed by Ahlers *et al.* [11] and Valencia *et al.* [17], and Ahlers *et al.* [11] in particular related them to changes in the viscous boundary layers as a result of viscosity variations. This can be illustrated by means of the momentum balance:

$$\bar{u}_j \frac{\partial \bar{u}_i}{\partial x_j} = -\frac{1}{\rho_0}\frac{\partial \bar{p}}{\partial x_i} - \frac{\bar{\rho}}{\rho_0} g \delta_{i3} + \frac{\partial}{\partial x_j}\left(\bar{\nu}\frac{\partial \bar{u}_i}{\partial x_j} + \overline{\nu' \frac{\partial u_i'}{\partial x_j}} - \overline{u_i' u_j'} \right). \tag{5.1}$$

In section 2.1.1 it was mentioned, that the third term on the right-hand side of the balance represents diffu-

sion of momentum. It is calculated as the gradient of the viscous stress, which scales with the local viscosity and the spatial derivatives of velocity. In general, the local flow is expected to arrange in such a way that the total amount of stress is minimized. To investigate, differences between the distributions of normalized viscosity in both cases are shown in figure 5.5. They are accompanied by changes in the vertical derivative of the velocity in the y-direction, the dominant velocity gradient component near the top and bottom walls.

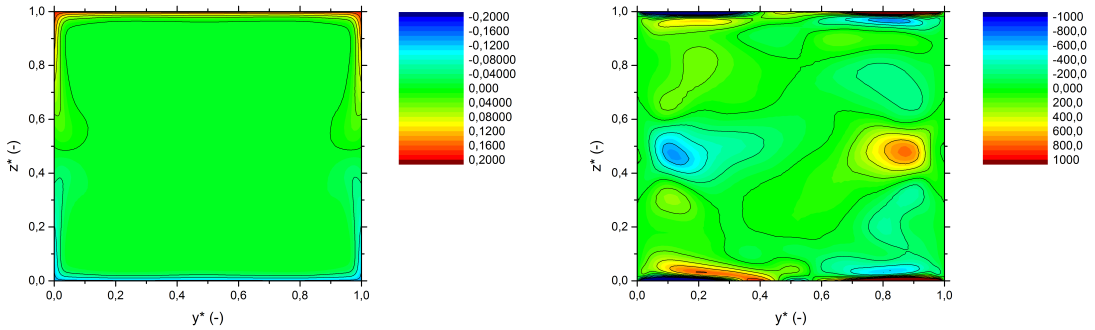

(a) Changes Δ in viscosity in the plane $x^* = 0.5$.

(b) Changes Δ in dv^*/dz^* in the plane $x^* = 0.5$.

Figure 5.5: Dimensionless changes Δ in viscosity and in the vertical derivative of v^*.

The changes in the vertical derivative at the walls are of the same order as the changes in viscosity (±15%) at those locations, but of differing sign. They result in an increase of the velocity gradient magnitude at the bottom wall, and a decrease at the top wall. In other words, the local velocity gradient at the wall adapts to the viscosity changes in such a way that it counteracts changes in the viscous stress. Based on this adaptation, one would expect to see minimal differences in the diffusion of momentum at the top and bottom walls. However, other characteristics of the flow should change as a result of the change in the velocity gradient, some of which were already observed in the velocity profiles. In order to get an understanding of the effects in terms of transport phenomena, the individual components of the momentum balance can be calculated. Generally, adaptations of the flow field are best studied by means of the advection, diffusion and turbulent transport terms. Because changes in pressure, buoyancy and fluctuations in viscosity are insignificant in the bulk, changes in the other terms should sum up to zero there, in order to preserve the momentum balance:

$$\begin{array}{llll} -\Delta \bar{u}^*{}_j \dfrac{\partial \bar{u}^*{}_i}{\partial x^*_j} & +\Delta \dfrac{\partial}{\partial x^*_j} \dfrac{\bar{\nu}}{\alpha_0} \dfrac{\partial \bar{u}^*{}_i}{\partial x^*_j} & -\Delta \dfrac{\partial}{\partial x^*_j} \overline{u^*{}'_i u^*{}'_j} & \approx 0, \\ \Delta\text{Advection} & +\Delta\text{Diffusion} & +\Delta\text{Turbulent transport} & \approx 0, \end{array}$$

where the mean thermal diffusivity α_0 is used to nondimensionalize the diffusion term. In order to quantify this balance, each term is calculated throughout the planes $x^* = 0.5$ and $z^* = 0.5$. First, changes in the diffusion term are studied, in order to verify the assumption that the viscous stress at the top and bottom remains largely unaltered. Figure 5.6 shows the dimensionless diffusion of y- and z-momentum for case 3, and its changes towards case 5.

The plots on the left-hand side illustrate that diffusion of momentum is of maximum magnitude near the walls, where the corresponding velocity gradient is at a maximum or minimum. As was mentioned before, viscous stress is most relevant in the equation for y-momentum in the region where the viscosity deviations manifest. Evidently, the plot of changes in diffusion of y-momentum supports the aforementioned prediction that adaptation of the velocity gradient counteracts changes in the viscous stress. The largest changes in terms of magnitude are of the order of ±10%, but confined to such small volumes that they are not significant. On the other hand, there is a significant increase of diffusion at the sidewalls near the vertical center. This is related to the increased downward velocity adjacent to that region: negative vertical momentum is diffused away from the walls into the downward flow. By the aforementioned balancing mechanism, changes are also expected to show up in this region in the advection and turbulent transport term of the equation for vertical momentum. Most illustrative are the changes in turbulent transport of vertical momentum, for which a plot is shown in figure 5.7.

The first plot is explanatory to the function of turbulent transport: it transports momentum in the direction of decreasing amounts of turbulence. In the case of RB-convection, most of the turbulent motion resides

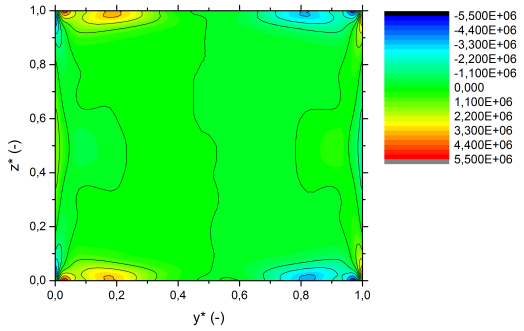

(a) Diffusion of y-momentum for case 3.

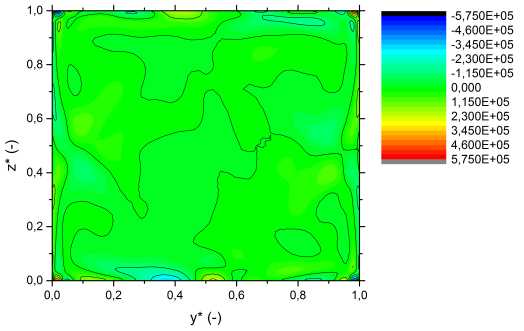

(b) Changes Δ in diffusion of y-momentum.

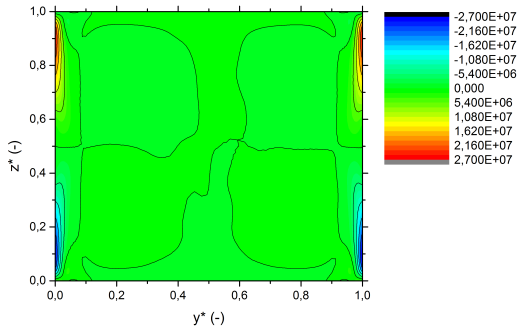

(c) Diffusion of z-momentum for case 3.

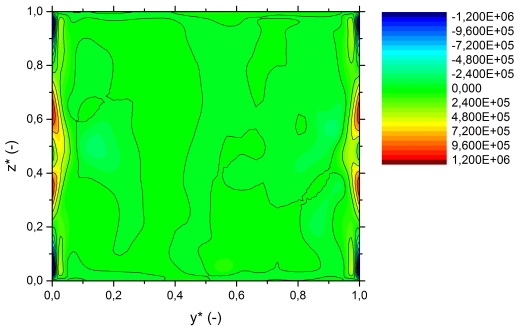

(d) Changes Δ in diffusion of z-momentum.

Figure 5.6: Dimensionless diffusion of momentum in the plane $x^* = 0.5$ for case 3, and changes towards case 5.

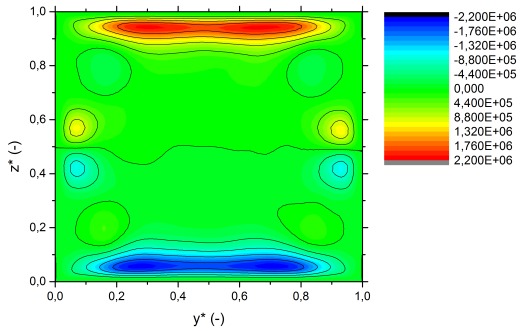

(a) Turbulent transport of z-momentum for case 3.

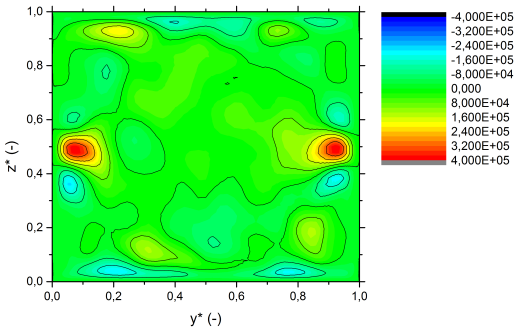

(b) Changes Δ in turbulent transport of z-momentum.

Figure 5.7: Dimensionless turbulent transport of vertical momentum in the plane $x^* = 0.5$ for case 3, and changes towards case 5.

in the bulk flow. This is also evident from the plot: downward momentum is transported from the bulk toward the bottom wall, and upward momentum is transported to the top wall. In the change towards case 5, the magnitude of this transport is increased near the bottom wall, and decreased near the top wall. Additionally, a significant amount of turbulent transport through the vertical center near the sidewalls is induced. The latter equals approximately 20% of the local turbulent transport maxima near the top and bottom walls. Both of the changes indicate that the amount of vertical turbulent motion is increased in the lower half and decreased in the upper half, causing a net increase of upward turbulent transport. As was mentioned in section 2.1.3, the total amount of local kinetic turbulence can be measured by means of the turbulence kinetic energy (TKE, e). In order to verify the preceding assumption, its distribution is calculated (see figure 5.8).

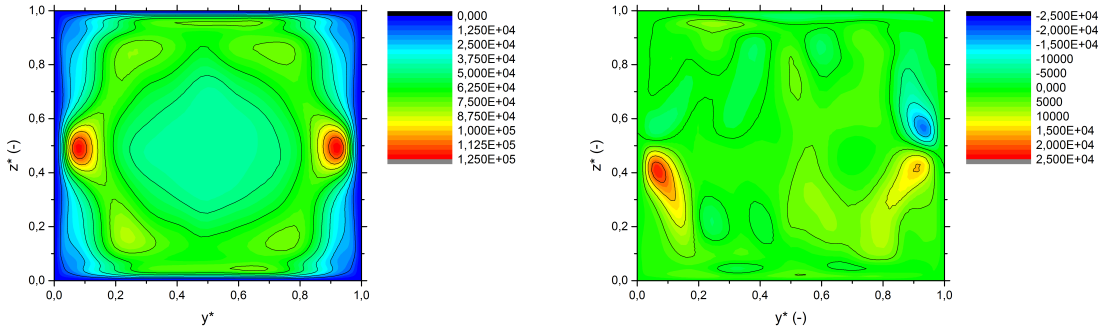

(a) Turbulence kinetic energy for case 3.

(b) Changes Δ in turbulence kinetic energy.

Figure 5.8: Dimensionless turbulence kinetic energy in the plane $x = 0.5$ for case 3, and changes towards case 5.

The left-hand sided plot shows that most of the turbulent motion indeed resides in the bulk flow, and the highest value of TKE is found inbetween the two toroidal vortices and the sidewalls. Again, an OB approximation would require perfect vertical symmetry, with TKE therefore distributed evenly between the upper and lower half of the cavity. The distribution in case 3 conforms quite well to this requirement. Furthermore, the plot on the right-hand side shows a net increase of TKE in the lower half and a net decrease in the upper half. The largest differences are found directly above and below the region where the actual amount of TKE is at its maximum. In this region, the fluctuations in the vertical velocity component are dominant, which is in good agreement with the changes in turbulent transport of vertical momentum. Possibly, more turbulence is generated in the lower half and vice versa for the upper half. Section 2.1.3 explained that the production of TKE scales with the local velocity gradient:

$$P = -\overline{u_i' u_j'} \frac{\partial \bar{u}_i}{\partial x_j}. \tag{5.2}$$

Production of TKE is therefore expected to be at its maximum in regions where the magnitudes of the velocity gradients are too, in this case near the cavity walls. It is also evident that when the magnitude of the local velocity gradient is altered, so is the production of turbulence kinetic energy. Qualitatively speaking, a decrease in viscosity at the bottom wall should on average increase the magnitude of the local velocity gradients, and therefore the production of TKE (and vice versa for the upper half). In order to quantify the changes, the amount of TKE can be averaged over a volume:

$$< e >= \frac{1}{2} \iiint_V \overline{u^*}_i'^2 \, dx^* \, dy^* \, dz^*. \tag{5.3}$$

The amount of TKE is averaged over both the upper and lower half of the cavity, and the results are given in table 5.2.

Volume	Case 3	Case 5	Δ
Lower half	8.13×10^4	8.68×10^4	$+5.5 \times 10^3 (+6.77\%)$
Upper half	7.91×10^4	7.81×10^4	$-1.0 \times 10^3 (-1.26\%)$
Full cavity	8.02×10^4	8.25×10^4	$+2.3 \times 10^3 (+2.87\%)$

Table 5.2: Averaged dimensionless turbulence kinetic energy for cases 3 and 5.

Evidently, the calculations confirm the vertical asymmetry of the distribution. Interestingly, the increase of mean TKE in the lower half is more significant than the decrease in the upper half. In any case, these changes should induce a net amount of turbulent transport through the vertical midplane. Furthermore, because vertical momentum is a conserved quantity, the upward turbulent transport must be compensated. As is known from figure 5.6, diffusion of vertical momentum is relatively small in the region of interest. Therefore, by the aforementioned balance, advection is expected to account for most of the compensation. To

verify this, changes in the vertical turbulent transport and advection terms in the balance for vertical momentum are calculated throughout the plane $z^* = 0.5$. The other terms do not contribute to the flux through that plane, and are therefore not of interest here. The results are shown in figure 5.9.

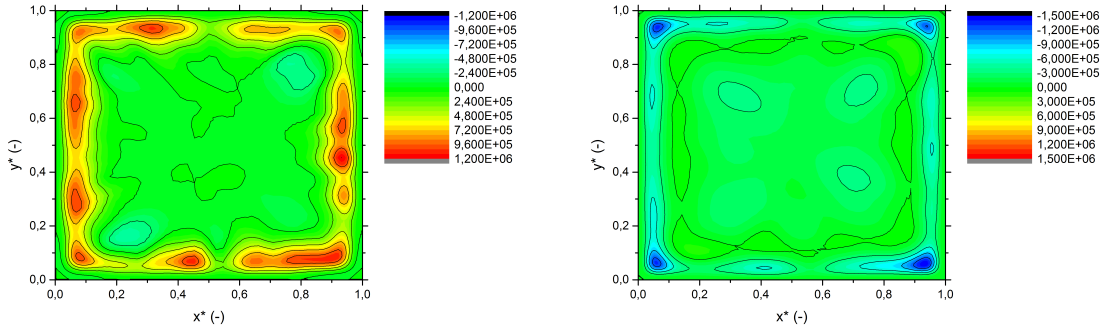

(a) Changes Δ in vertical turbulent transport of z-momentum.

(b) Changes Δ in vertical advection of z-momentum

Figure 5.9: Dimensionless changes in vertical turbulent transport and advection of z-momentum in the plane $z = 0.5$.

These plots support the presumed mechanism: the surplus of turbulent momentum in the lower half induces a net turbulent transport through the vertical midplane, which is most significant near the walls, where turbulence is at its maximum. Downward advection is increased in the same regions, so that the momentum balance is preserved. Diffusive transport in the vertical direction is increased in a similar vane as turbulent transport, but its net contribution is negligible when compared to the other two terms. In order to arrive at some form of quantification of the net contributions and verify the balance, each transport term is averaged throughout the plane:

$$< \text{Advection} > = - \iint_S \bar{w}^* \frac{\partial \bar{w}^*}{\partial z^*} dx^* dy^*, \tag{5.4}$$

$$< \text{Diffusion} > = \iint_S \frac{\partial}{\partial z^*} \frac{\bar{\nu}}{\alpha_0} \frac{\partial \bar{w}^*}{\partial z^*} dx^* dy^*, \tag{5.5}$$

$$< \text{Turbulent transport} > = - \iint_S \frac{\partial}{\partial z^*} \overline{w^{*\prime 2}} dx^* dy^*. \tag{5.6}$$

The results of this calculation are given in table 5.3.

Component	Case 3	Case 5	Δ
< Advection >	-6.9×10^4	-3.0×10^5	-2.3×10^5
< Diffusion >	$+7.8 \times 10^2$	$+5.5 \times 10^3$	$+4.7 \times 10^3$
< Turbulent transport >	$+7.2 \times 10^4$	$+3.0 \times 10^5$	$+2.3 \times 10^5$
Total	$+3.9 \times 10^3$	$+1.1 \times 10^4$	$+7.3 \times 10^3$

Table 5.3: Averaged dimensionless momentum transport terms and differences for cases 3 and 5.

The changes in advection indeed appear to balance out the induced increase in turbulent transport: the changes towards case 5 are of the exact same magnitude and opposing sign. The average increase in turbulent transport at the vertical center is approximately 10% of the local maxima in figure 5.7. For a proper quantification of the differences in transport contributions on a global scale, the magnitude of the components can be averaged over the entire cavity. Although that was beyond the scope of this project, it was possible to quantify the relative changes in mean kinetic energy E, analogously to the calculation for TKE:

$$< E >= \frac{1}{2} \iiint_V \bar{u}^{*2}_i dx^* dy^* dz^*, \tag{5.7}$$

where the normalized density is approximated by 1. The results are presented in table 5.4.

Volume	Case 3	Case 5	Δ
Lower half	1.386×10^5	1.385×10^5	$-0.1 \times 10^3 (-0.07\%)$
Upper half	1.403×10^5	1.420×10^5	$+1.7 \times 10^3 (+1.21\%)$
Full cavity	1.395×10^5	1.403×10^5	$+0.8 \times 10^3 (+0.57\%)$

Table 5.4: Averaged dimensionless mean kinetic energy for cases 3 and 5.

As is evident from these results, the absolute increase in mean kinetic energy is of the same order as the increase in TKE, which is to be expected. However, most of the total kinetic energy is contained in the mean velocity, and so the relative increase in mean kinetic energy is much smaller than that of TKE. This is in good agreement with the observed qualitative differences in actual fluid motion: the relative changes in the mean velocity field are small compared to the relative changes in the distribution of turbulence. In any case, the increased property variations do induce a net increase of fluid motion, which should have a positive effect on heat transport. The following section will discuss the changes to heat transfer, and feature a similar analysis of these contributions.

5.1.3. EFFECTS ON HEAT TRANSFER

As was mentioned before, Ahlers *et al.* [11] found asymmetries in the vertical NOB-temperature profiles: their experimental time-averaged temperatures at the vertical center of a cylindrical geometry were higher than the arithmetic mean of the temperatures at the top and bottom walls. In order to confirm this characteristic, temperature profiles along the line $x^* = 0.5$, $y^* = 0.5$ are presented in figure 5.10, along with the temperature distribution in the y-z centerplane for case 5.

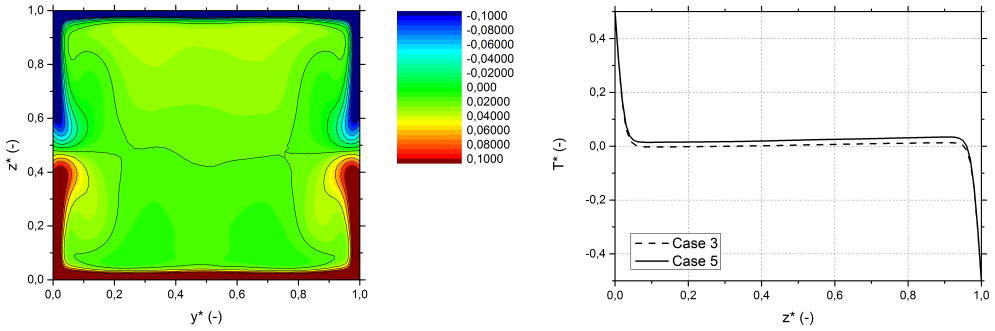

(a) Temperature in the plane $x^* = 0.5$ for case 5.

(b) Temperature along the line $x^* = 0.5$, $y^* = 0.5$.

Figure 5.10: Dimensionless time-averaged temperature profiles for cases 3 and 5.

These profiles are in agreement with the asymmetries found by Ahlers *et al.* [11]: the bulk temperature is approximately 0.02 nondimensional units higher than the arithmetic mean for case 5. On the other hand, the temperature profile in case 3 is close to antisymmetric. Apparently, property variations induce increased heat transfer from the bottom wall to the bulk, and vice versa for the top wall. Analogous to the preceding discussion of fluid motion, a term-by-term analysis of the heat balance is done to investigate what is happening. The balance equation is given by:

$$\bar{u}_j \frac{\partial \bar{T}}{\partial x_j} = \frac{\partial}{\partial x_j} \left(\bar{\alpha} \frac{\partial \bar{T}}{\partial x_j} + \overline{\alpha' \frac{\partial T'}{\partial x_j}} - \overline{u'_j T'} \right). \tag{5.8}$$

Fluctuations in diffusivity are found to be negligible, so changes in advection, diffusion and turbulent transport are expected to balance out:

$$\underbrace{-\Delta \bar{u}^*{}_j \frac{\partial \bar{T}^*}{\partial x^*_j}}_{\Delta\text{Advection}} \quad \underbrace{+\Delta \frac{\partial}{\partial x^*_j} \frac{\bar{\alpha}}{\alpha_0} \frac{\partial \bar{T}^*}{\partial x^*_j}}_{+\Delta\text{Diffusion}} \quad \underbrace{-\Delta \frac{\partial}{\partial x^*_j} \overline{u^{*\prime}{}_i T^{*\prime}}}_{+\Delta\text{Turbulent transport}} \quad \underbrace{\approx 0,}_{\approx 0.}$$

Because the variations in thermal diffusivity are small, they do not have a significant effect through the thermal diffusion term. On the other hand, it was shown that the changes in viscosity induce a significant alteration of the velocity gradient at the top and bottom walls. It appears that thermal diffusion, which is mainly active in those regions, is also affected. The distribution of thermal diffusion and its changes are shown in figure 5.11.

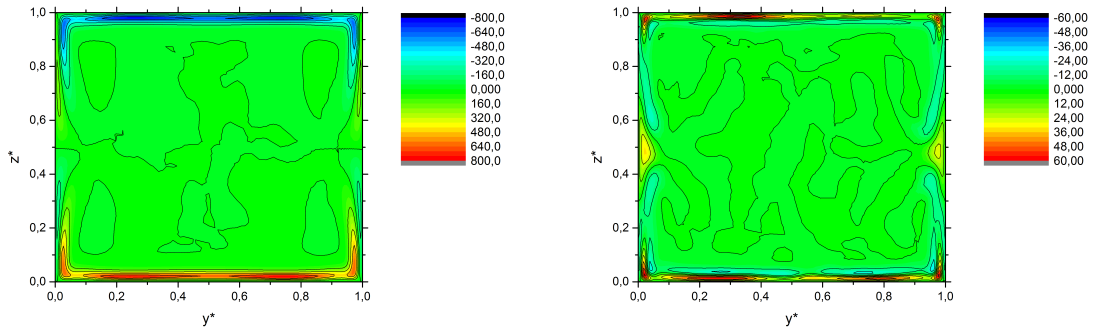

(a) Thermal diffusion for case 3.

(b) Changes Δ in thermal diffusion.

Figure 5.11: Dimensionless thermal diffusion in the plane $x = 0.5$ for case 3, and changes towards case 5.

The first plot illustrates that thermal diffusion is indeed most active near the walls. The changes that occur near the top and bottom walls, are approximately ±7.5% of the total diffusion at that location, and can be related to the alterations of the local velocity gradient. Because the velocity gradient magnitude is increased at the bottom wall and decreased at the top wall, the bulk flow is displaced towards the bottom wall. This allows for more heat to diffuse from the bottom wall into the bulk, and less to diffuse from the bulk to the top wall. As a result, the mean temperature gradient remains largely unaffected, and the bulk temperature is increased. Seeing as the changes in diffusion are of equal magnitude and opposing direction, they largely balance out one another. Therefore, the resulting effect on heat transfer should be negligible. Furthermore, there appears to be a net increase in temperature by diffusive transport near the sidewalls at the vertical center. This should be related to the bulk temperature becoming higher than the arithmetic mean, which is also the temperature of the sidewalls at the vertical center. Additionally, the increased mixing might have an amplifying effect on the diffusive transport in this region. Based on the discussion of momentum transport, more significant changes are expected in the turbulent transport and advection terms, which are calculated and shown in figure 5.12.

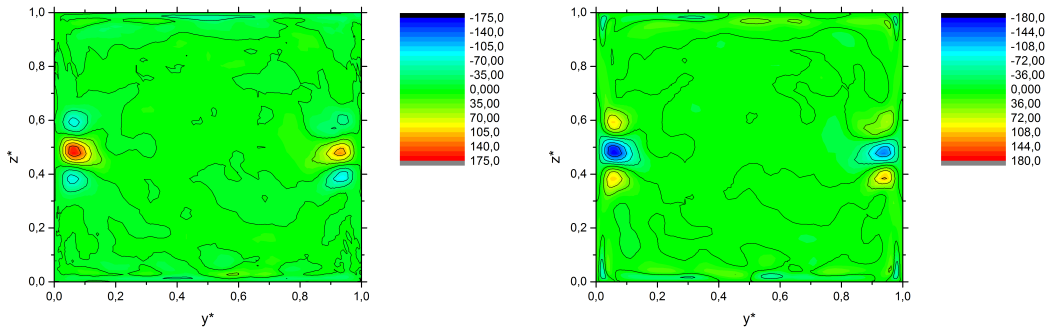

(a) Changes Δ in turbulent transport of heat.

(b) Changes Δ in advection of heat.

Figure 5.12: Changes in dimensionless turbulent transport and advection of heat in the plane $x = 0.5$.

Evidently, the changes in both the turbulent transport and the advection terms are most significant in the region where the changes in their counterparts for vertical momentum were affected. The explanation is analogous: the excess of turbulence just below the vertical center near the sidewalls induces a net turbulent

flux through the vertical centerplane, which is compensated for by an approximately equal advection term of opposite sign. In other words: the upward turbulent transport of heat creates a positive spatial derivative of temperature in that direction, which induces downward advective transport. It should be noted that turbulent transport and advection of heat are also proportional to the temperature gradient, and are therefore active inside the thermal boundary layer. Because fluid motion in that region is altered, one might expect to see changes in these terms as well. However, fluid motion is mostly affected in the horizontal directions, and in those directions the temperature gradient is negligible. On average, the most significant changes in net heat transfer seem to be a result of the increased mixing in the region near the sidewalls at the vertical center. Like before, the vertical components of advection and turbulent transport of heat are calculated at $z^* = 0.5$ and shown in figure 5.13.

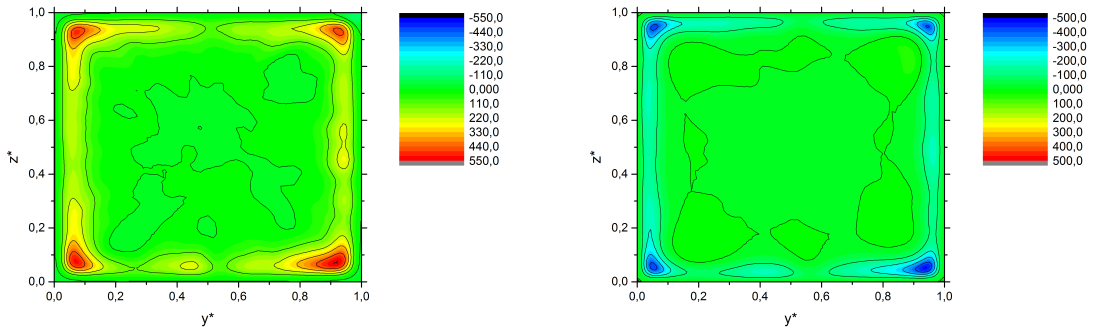

(a) Changes Δ in turbulent transport of heat.

(b) Changes Δ in advection of heat.

Figure 5.13: Changes in dimensionless turbulent transport and advection of heat in the plane $z = 0.5$.

These plots are similar to their counterparts for momentum transport. There is a significant increase of turbulent transport through the vertical center, which is counteracted by an increase of advection. Again, all components are averaged over the plane in order to get some form of quantification.

$$< \text{Advection} >= -\iint_S \bar{w}^* \frac{\partial \bar{T}^*}{\partial z^*} dx^* dy^*, \tag{5.9}$$

$$< \text{Diffusion} >= \iint_S \frac{\partial}{\partial z^*} \frac{\bar{\alpha}}{\alpha_0} \frac{\partial \bar{T}^*}{\partial z^*} dx^* dy^*, \tag{5.10}$$

$$< \text{Turbulent transport} >= -\iint_S \frac{\partial}{\partial z^*} \overline{w^{*\prime} T^{*\prime}} dx^* dy^*. \tag{5.11}$$

Note here, that there is a net diffusive heat flux directed towards the sidewalls. Therefore, the vertical transport terms for heat are not expected to cancel out completely. Instead, they should sum up to a net deficit. The results of this integration are given in table 5.5.

Component	Case 3	Case 5	Δ
< Advection >	−23.7	−94.5	−70.8
< Diffusion >	+2.3	+9.3	+7.0
< Turbulent transport >	+31.6	+120.5	+88.9
Total	+10.2	+35.3	+25.1

Table 5.5: Averaged dimensionless vertical heat transport terms and differences for cases 3 and 5.

These results again confirm the mechanism that was described in the previous section: there is a significant net increase in upward turbulent transport, combined with a net increase of downward advection. It appears that the diffusive transport towards the walls is significant, because the net deficit is too. In any case, the induced transport of momentum and heat through the vertical midplane should have a net positive effect on the total amount heat transfer through the system. In order to quantify the presumed increase, the Nusselt number was calculated for both cases according to the equation presented in section 2.1.4: its value

was 11.6 for case 3 and 11.7 for case 5. This comes down to an increase of 0.9%, which is in agreement with the findings by Valencia *et al.* [17]. A qualitative argument can be made for this relative change. The induced changes in diffusive transport through the boundary layers are likely to cancel out one another. Ahlers *et al.* [11] in particular mentioned that the total thickness of the thermal boundary layers is not affected, and as a result, neither is the heat transport through them. Additionally, the more significant changes in mixing due to turbulent and advective transport are directly related to mean kinetic and turbulence kinetic energy. Therefore, the net increase in heat transfer can be expected to be of the same order as the changes in total kinetic energy, which is indeed the case.

5.2. CASE 6 VERSUS CASE 7

Following is a comparison between the OB and NOB case that were intended as a numerical reproduction of an in-house experimental study by Valentina Valori. The specifics of these cases are given once more in table 5.6. Note that there is a difference in Rayleigh number of 2.5%, and also a significant difference in Prandtl number. In addition, chapter 3 explained that the numerical resolution is in theory too low to resolve all turbulent length scales for these cases. That means that a direct quantitative comparison between these cases would be very complicated, and therefore conclusions should only be drawn based on qualitative aspects of the comparison. As before, Δ is used to denote the changes of a dimensionless quantity in case 6 towards its counterpart in case 7, e.g. $\Delta\Phi^* = \Phi^*_7 - \Phi^*_6$.

Parameter	Case 6	Case 7
Fluid	methanol	water
OB/NOB	OB*	NOB
Ra	6.74×10^8	6.91×10^8
Pr	7.23	4.08
H (m)	0.077	0.077
T_s	adiabatic	adiabatic
ΔT (K)	9.6	40
$\Delta\rho$ (%)	1.04	1.53
$\Delta\beta$ (%)	49.1	87.7
$\Delta\mu$ (%)	14.4	87.9
$\Delta\lambda$ (%)	3.16	7.14
Δc_p (%)	0.17	0.17

Table 5.6: Specifications of cases 6 and 7.

5.2.1. DISTRIBUTION OF PROPERTY VARIATIONS

Again, the distribution of property variations is investigated in order to predict the qualitative local influences. Analogous to before, the main interest lies with the effects induced by viscosity variations. Its time-averaged and instantaneous distribution are presented in figure 5.14.

As was the case in the previously discussed distributions, the time-averaged viscosity deviations are largely confined to the thermal boundary layers. However, the average viscosity in the bulk is roughly 3% lower than the arithmetic mean, because the bulk temperature is also significantly higher than the mean temperature T_0. In addtion, there appears to be a horizontal asymmetry in the viscosity distribution, which translates to asymmetries in the horizontal temperature profile. The variations seen in the instantaneous profile are of the order of $\pm$10%.

5.2.2. EFFECTS ON FLUID MOTION

The flow structure is again the same for both cases. It contains a single roll that is clockwise in the diagonal in the plane $x^* = 0.5$, and diagonal in the horizontal and vertical centerplanes, accompanied by small rolls in opposing corners of the cavity. The complete structure is antisymmetrical with respect to the planes $x^* = 0.5$ and $y^* = 0.5$. Figure 5.15 shows the velocity magnitude in the horizontal and vertical centerplanes for case 7, followed by its changes towards case 7.

There is a significant increase in velocity magnitude along the bottom wall. Based on the preceding discussion of the adaptation of velocity gradients, this change is expected. However, it appears that there is now

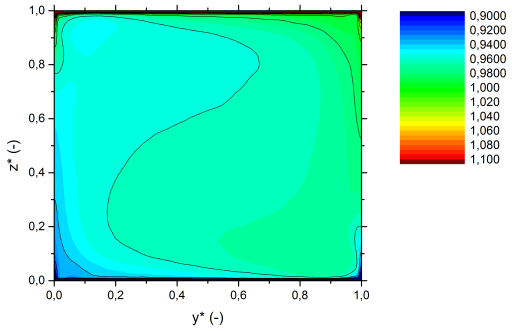

(a) Time-averaged distribution.

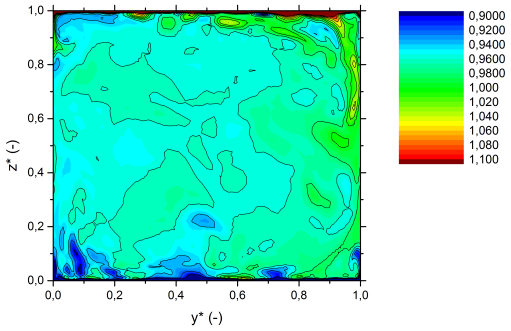

(b) Instantaneous distribution.

Figure 5.14: Normalized viscosity in the plane $x = 0.5$ for case 7.

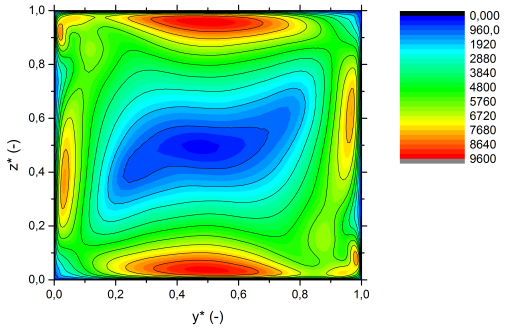

(a) Velocity magnitude in the plane $x^* = 0.5$.

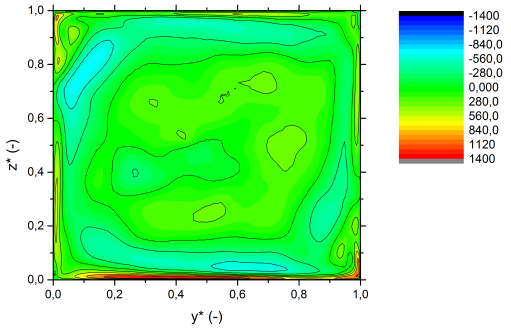

(b) Changes Δ in velocity magnitude in the plane $x^* = 0.5$.

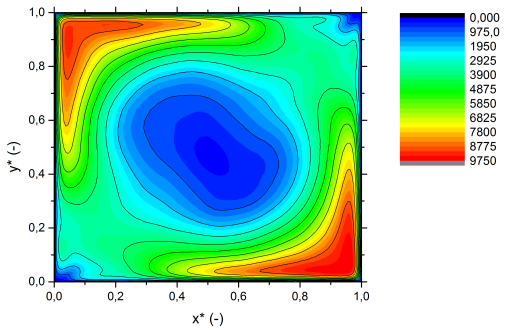

(c) Velocity magnitude in the plane $z^* = 0.5$.

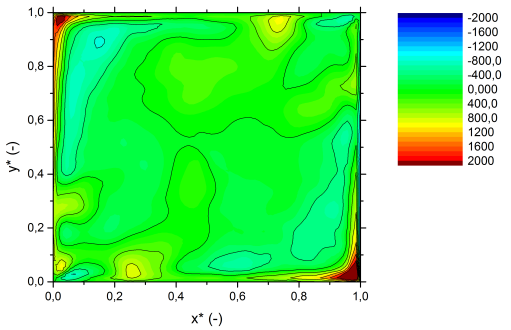

(d) Changes Δ in velocity magnitude the plane $z^* = 0.5$.

Figure 5.15: Velocity magnitude in the horizontal and vertical centerplanes for case 7, followed by its changes towards case 7.

also an increased velocity magnitude along the top wall, which seems to contradict that same discussion. Furthermore, there is a large increase in vertical velocity magnitude through the upper left and lower right corner of the vertical centerplane. The magnitude is also increased in the center region of the bulk flow, and it is decreased further towards the wall. The changes in the bulk flow are of the order of $\pm 5\%$, and the increase of magnitude along the walls are approximately 10 to 20%. Following the analysis in the previous section, the effects on turbulent motion are investigated. Figure 5.16 presents the distribution of TKE for case 6, followed by its changes towards case 7.

Based on the increased velocity magnitude along the walls in the preceding plots, one would expect that the production of TKE along these walls is increased. Evidently, the changes in the distribution of TKE support

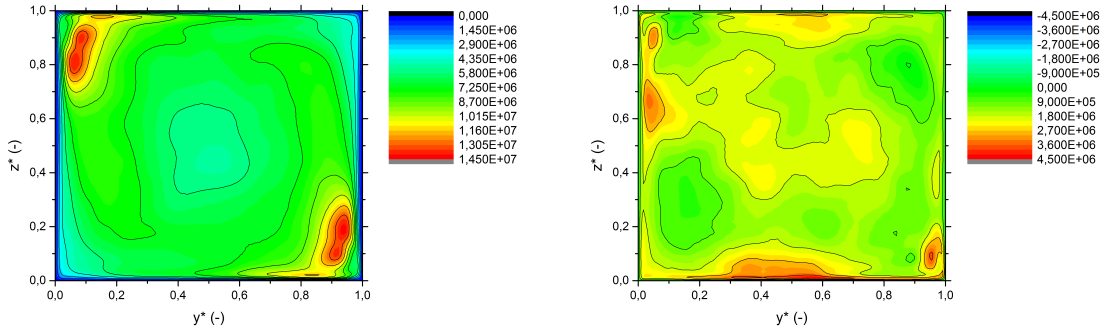

(a) Turbulence kinetic energy for case 6.

(b) Differences Δ in turbulence kinetic energy.

Figure 5.16: Dimensionless turbulence kinetic energy in the y-z centerplane for case 6, and the changes towards case 7.

this claim, as the value of TKE is increased significantly throughout the entire plane. The maximum local increase is of the order of 30%, but in order to quantify the global changes the value of TKE must be averaged over the cavity. The results of this integration are given in table 5.7. Note that this quantification can prove to be inaccurate because of the lacking numerical resolution, large differences can be indicative of a qualitative trend.

Volume	Case 6	Case 7	Δ
Lower half	7.52×10^6	9.00×10^6	$+1.48 \times 10^6 (+19.7\%)$
Upper half	7.46×10^6	9.03×10^6	$+1.57 \times 10^6 (+21.0\%)$
Full cavity	7.49×10^6	9.02×10^6	$+1.53 \times 10^6 (+20.4\%)$

Table 5.7: Averaged dimensionless turbulence kinetic energy for cases 6 and 7.

It appears that, although the total amount of turbulent motion is significantly increased, there is actually a slight decrease in difference between the upper and lower half. Seeing as the increase in velocity magnitude is significantly greater at the bottom wall than at the top wall, one could argue that the production of TKE should change accordingly, and that the amount of TKE in the lower half should become higher than that in the upper half. Apparently this is not the case; a possible explanation being that mixing by the mean flow is increased for this higher Rayleigh number, and that TKE is therefore distributed more evenly throughout the cavity. In order to find out what the specific impact of these changes is, it is possible to calculate the local turbulent transport of momentum. However, such an analysis would not be very trustworthy because of the lacking numerical resolution, and is in any case beyond the scope of this investigation. Instead, the volume-averaged mean kinetic energy is calculated for comparison, and the results are given in table 5.8.

Volume	Case 6	Case 7	Δ
Lower half	1.252×10^7	1.232×10^7	$-2.0 \times 10^5 (-1.60\%)$
Upper half	1.263×10^7	1.214×10^7	$-4.9 \times 10^5 (-3.88\%)$
Full cavity	1.258×10^7	1.223×10^7	$-3.5 \times 10^5 (-2.78\%)$

Table 5.8: Averaged dimensionless mean kinetic energy for cases 6 and 7.

Interestingly, there is a decrease of mean kinetic energy throughout the cavity. Also, the difference between the upper and lower half is increased. Further research would be necessary to explain these changes and properly predict their consequences. The following section will present a brief analysis of the resulting effects in terms of heat transfer.

5.2.3. EFFECTS ON HEAT TRANSFER

A qualitative analysis of the influence of NOB effects on heat transfer is conducted by comparing vertical temperature profiles and the average Nusselt number. The time-averaged temperature distribution for both cases is shown in figure 5.17.

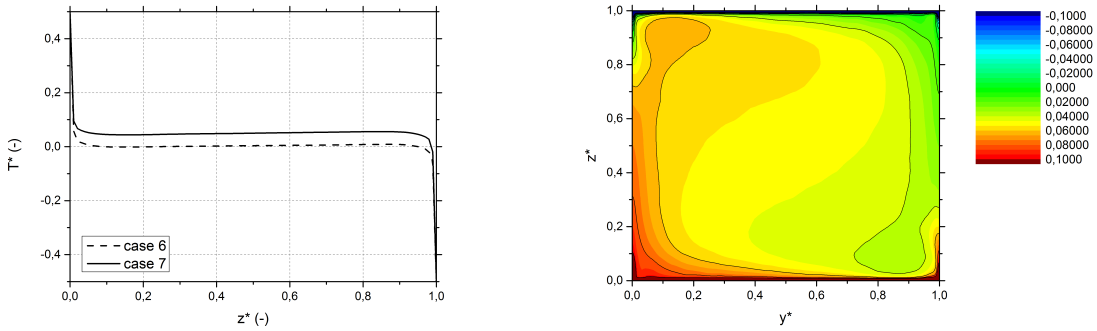

(a) Temperature profiles along the vertical axis.

(b) Temperature in the plane $x^* = 0.5$ for case 7.

Figure 5.17: Dimensionless time-averaged temperature profiles for cases 6 and 7.

As was the case in the preceding discussion of cases 3 and 5, the NOB effects induce an increase in bulk temperature. This effect is even greater for cases 6 and 7 and also significantly asymmetrical: the time-averaged dimensionless temperature is around 0.07 near the left sidewall, and 0.05 in the center of the bulk. This effect is probably caused by the same mechanism that was discussed in the previous comparison, with upward diffusion being increased at the bottom wall and decreased at the top wall. However in this case, the increase of velocity magnitude on both sides should imply that diffusion through the boundary layers is increased on both sides. It would appear that the increase in the bottom boundary layer is significantly larger, and the bulk temperature is again increased. As was explained, a term-by-term analysis of these cases was beyond the scope of this project. In order to quantify the net effect on heat transfer, the Nusselt number was calculated for both cases. Its value was 62.4 for case 6, and 62.6 for case 7: an increase of 0.3%, which is in line with the previous findings for lower Rayleigh numbers.

5.3. FINAL REMARK WITH REGARD TO HEAT TRANSFER

As was mentioned before, the Rayleigh number and Prandtl number were different for these latter two cases. Therefore, no direct correlation of the property variations with the changes in total heat transfer can be established based on these results. However, it is safe to conclude that there is no significant vertical symmetry breaking in the distribution of TKE due to increased viscosity variations at the highest investigated Rayleigh number. Also, it is known from the literature by Ahlers *et al.* [11, 18] and Valencia *et al.* [17] that the positive effect of viscosity variations on heat transfer diminishes as the Rayleigh number is increased. From the previous comparison it could be deduced that there is a strong correlation between the symmetry breaking in the distribution of TKE, and the increased heat transport due to turbulence. Therefore, the general hypothesis is formulated that the symmetry breaking in the distribution of TKE due to viscosity variations is reduced for higher Rayleigh numbers, and that this causes the positive effect of viscosity variations on heat transfer to decrease. This is a different approach than that taken by Ahlers *et al.* [11], who related the decreased effect to turbulence in the thermal boundary layers (although these explanations are not mutually exclusive). More research is necessary for a complete understanding of this aspect.

6

CONCLUSIONS AND RECOMMENDATIONS

This chapter presents the reader with the key conclusions of the investigation. Subsequently, recommendations for future research are given.

6.1. CONCLUSIONS

In agreement with the investigation goals, turbulent Rayleigh-Bénard (RB) convection was simulated in a fluid in a cubical cavity, under Non-Oberbeck-Boussinesq (NOB) circumstances and at two different Rayleigh numbers. These circumstances induced significant local variations in thermophysical properties, most importantly in the viscosity of the fluid. The simulations were compared qualitatively and quantitatively with two other simulations at the same Rayleigh number, in which the corresponding thermophysical properties did not vary significantly. In that way, the isolated influence of the property variations could be conveniently studied. Following are the conclusions that were derived from the comparison at the lowest of the two Rayleigh numbers.

- The first comparison was conducted at a Rayleigh number of 10^7. The temperature difference between the top and bottom cavity walls was 4.07K in the first case and 16.6K in the second, resulting in viscosity variations of approximately ±5% and ±20%, respectively. It was found that, in agreement with literature, these variations were mostly confined to the thin thermal boundary layers at the top and bottom walls of the cavity. Therefore, on average, there were no significant viscosity variations in the bulk flow.

- The time-averaged flow structure consisted of two toroidal rolls, one in each vertical half of the cavity, as was described by Valencia *et al.* [3]. This flow structure was not altered significantly as a result of the increased property variations. However, a closer look at the velocity field revealed that there were notable changes.

- The decrease in viscosity at the bottom wall, resulted in an equal relative increase of the local velocity gradient magnitude (and vice versa for the top wall). This induced a vertical shift in the velocity profile. In the case where viscosity variations were negligible, the velocity profile was close to symmetrical in the vertical direction. Therefore, the vertical shift as a result of viscosity variations translates to a breaking of vertical symmetry. This characteristic was also observed and explained by Ahlers *et al.* [11].

- As a result of the changes in velocity gradient magnitude at the top and bottom walls, the production of turbulence kinetic energy (TKE) was altered. The average value of TKE in the lower half was increased by 6.77% and in the upper half it was reduced by 1.26%, resulting in a net increase of TKE by 2.87%. There was also a net decrease of mean kinetic energy in the lower half by 0.07% and a net increase in the upper half by 1.21%, so that the total amount was increased by 0.57%.

- The largest vertical differences in TKE were found close to the vertical center, near the sidewalls. The asymmetry in the distribution of TKE induced a net upward flux of turbulent momentum transport through the vertical centerplane in the same region. This flux was compensated for by an equal and opposite advective flux in the same region.

- The induced advective and turbulent momentum flux through the vertical center translated to advective and turbulent transport of heat at the same location. This advective and turbulent transport is presumed to have a net positive effect on heat transfer through the system.

- The vertical displacement of the bulk flow also induced an increase of upward thermal diffusion through the bottom boundary layer and an approximately equal decrease of diffusion through the upper boundary layer. As a result the temperature in the bulk was increased by 2% of the temperature difference.

- The total amount of heat transfer was quantified in terms of the Nusselt number, which was increased by 0.9% as a result of property variations. The increase is most likely caused by the combination of induced advective and turbulent transport that follow from viscosity variation, and it is in agreement with the literature by Valencia *et al.* [17].

The following two cases were intended as a replication of experimental data by Valentina Valori. Although the numerical resolution of the simulations did not conform to the theoretical minimum for these cases, there was good agreement with the experimental data, as is illustrated in chapter 4. However, the comparison of these results was mainly focussed on finding qualitative differences, as opposed to conducting an accurate quantification. Following are the most notable conclusions from that analysis.

- The second comparison was made between a case at a Rayleigh number of 6.74×10^8 and a case at a Rayleigh number of 6.91×10^8. The temperature difference between the top and bottom cavity walls was 9.6K in the first case and 40K in the second, resulting in viscosity variations of approximately $\pm7\%$ and $\pm44\%$, respectively. Again, the variations were mostly confined to the thermal boundary layers.

- The time-averaged flow structure consisted of a single diagonal roll. Like before, the flow structure was not altered significantly by the property variations.

- As a result of the viscosity variations, the velocity magnitude at the bottom wall was increased by approximately 15%. However, the magnitude at the top wall was also increased slightly.

- The total amount of turbulence kinetic energy is increased by approximately 20%, and the total amount of mean kinetic energy was decreased by approximately 2.78%. However, both quantities are distributed more evenly throughout these cases, and therefore no significant breaking of vertical symmetry is induced.

- The mean dimensionless temperature in the bulk was increased by 5% of the temperature difference in this case. This could be related to changes in diffusive transport through the thermal boundary layers, similar to those observed before.

- The calculated Nusselt number was increased by 0.3% in the case of increased property variations. It should be noted that the Nusselt number is dependent on the Rayleigh number and the Prandtl number, both of which are different between the two cases. Therefore a direct relation to the viscosity variations is not evident. In a qualitative sense though, it can be said that the increase in heat transfer due to viscosity variations must be smaller at this Rayleigh number.

From the two comparisons, a new hypothesis with respect to the effect of viscosity variations on heat transfer can be formulated for further investigation:

- The increased heat transfer that occurs in the first comparison as a result of increased viscosity variations, could be directly related to the induced vertical symmetry breaking in the distribution of TKE. It is known from literature that this increase in heat transfer diminishes as the Rayleigh number goes up. The second comparison shows that the aforementioned symmetry breaking is not evident at a higher Rayleigh number. Therefore one could argue that the effect on heat transfer is decreased when the Rayleigh number goes up, because the induced symmetry breaking in the distribution of TKE due to viscosity variations is diminished.

6.2. RECOMMENDATIONS FOR FUTURE RESEARCH

This section lists some recommendations for the continuation of this investigation, and for research on the topic of NOB-effects in RB convection in general.

- In order to verify the hypothesis formulated above, a quantitative investigation of the direct relation between the distribution of TKE and heat transfer should be conducted. Ahlers *et al.* [11] also found a correlation with the distribution of TKE, but they related it with turbulence in the boundary layers. In order to investigate distributions of TKE should be generated for different amounts of viscosity variation and throughout a range of Rayleigh numbers. It is possible to conduct this continuation with the code used in this investigation, although computational power must be added to properly simulate turbulence at higher Rayleigh numbers. It should also be noted, that property variations have an even greater effect on heat transfer at laminar Rayleigh numbers, where the relation with symmetry breaking in the distribution of TKE is not a possible explanation. Therefore, the mean kinetic energy can be investigated for those cases in order to look for a similar correlation.

- In the context of supercritical fluids, the code must be adapted to account for large density variations. This is not a very difficult task in terms of coding, but would require proper validation material for the flow type of interest. Ideally, the simulation of supercritical flow would be accompanied by corresponding in-house experimental data. Again, the simulations in this project were restricted to lower turbulent Rayleigh numbers by the available computational power. This should be taken into consideration when the adaptation to supercritical flow is made, because the required numerical resolution is even higher for supercritical fluids due to local extrema in the Prandtl number.

- As is evident from this investigation as well as from earlier studies, the boundary layer structure plays a very important role in the context of NOB-effects. The most significant property variations are on average confined to the thin thermal boundary layers at the top and bottom walls, which is an important restriction on their impact on the mean flow. In that regard, it might prove more useful to study these aspects in other types of enclosures with differing large scale dynamics. In a vertical pipe with a linear vertical derivative of temperature on the boundary, properties vary significantly thoughout the entire flow, and should show more interaction with the bulk flow.

A

REYNOLDS AVERAGING DERIVATIONS

This appendix provides a complete derivation of the Reynolds averaged versions for the partially simplified governing equations 2.10, 2.11, and 2.12:

$$\frac{\partial u_j}{\partial x_j} = 0, \tag{A.1}$$

$$\frac{\partial u_i}{\partial t} + u_j \frac{\partial u_i}{\partial x_j} = -\frac{1}{\rho_0}\frac{\partial p}{\partial x_i} - \frac{\rho}{\rho_0} g \delta_{i3} + \frac{\partial}{\partial x_j}\left(\nu \frac{\partial u_i}{\partial x_j}\right), \tag{A.2}$$

$$\frac{\partial T}{\partial t} + u_j \frac{\partial T}{\partial x_j} = \frac{\partial}{\partial x_j}\left(\alpha \frac{\partial T}{\partial x_j}\right). \tag{A.3}$$

Fluctuating variables can be decomposed into a mean (time-averaged) part and fluctuating part, denoted by an overline and a prime:

$$\Phi = \bar{\Phi} + \Phi', \tag{A.4}$$

$$\bar{\Phi} = \frac{1}{T}\int_{t-T/2}^{t+T/2} \Phi dt, \tag{A.5}$$

with Φ the instantaneous value of the output variable of choice, and T the averaging time. The averaging operator obeys a number of general rules (see Nieuwstadt [8]), for example that time-averaged non-linear terms drop out when a multiplication is averaged:

$$\begin{aligned}
f &= \bar{f} + f', \\
g &= \bar{g} + g', \\
\overline{fg} &= \overline{(\bar{f} + f')(\bar{g} + g')}, \\
\overline{fg} &= \overline{\bar{f}\bar{g} + \bar{f}g' + f'\bar{g} + f'g'}, \\
\overline{fg} &= \overline{\bar{f}\bar{g}} + \overline{\bar{f}g'} + \overline{f'\bar{g}} + \overline{f'g'}, \\
\overline{fg} &= \overline{\bar{f}\bar{g}} + \overline{f'g'}.
\end{aligned}$$

For the aforementioned governing equations, the variables that should be decomposed are:

$$\begin{aligned}
u_i &= \bar{u}_i + u_i', \\
p &= \bar{p} + p', \\
T &= \bar{T} + T', \\
\rho &= \bar{\rho} + \rho', \\
\nu &= \bar{\nu} + \nu', \\
\alpha &= \bar{\alpha} + \alpha'.
\end{aligned} \tag{A.6}$$

Substitution of these variables into the continuity equation, followed by averaging, yields :

$$\overline{\frac{\partial u_j}{\partial x_j}} = \frac{\overline{\partial(\bar{u}_j + u'_j)}}{\partial x_j} = \frac{\partial \bar{u}_j}{\partial x_j} = 0. \tag{A.7}$$

In the momentum equations, it is convenient to rewrite the advection terms by means of the instantaneous continuity equation, before decomposing:

$$u_j \frac{\partial u_i}{\partial x_j} = \frac{\partial u_i u_j}{\partial x_j} - u_i \frac{\partial u_j}{\partial x_j} = \frac{\partial u_i u_j}{\partial x_j}. \tag{A.8}$$

Decomposing and averaging leads to:

$$\begin{aligned} \overline{\frac{\partial u_i u_j}{\partial x_j}} &= \frac{\overline{\partial(\bar{u}_i + u'_i)(\bar{u}_j + u'_j)}}{\partial x_j} = \frac{\partial \bar{u}_i \bar{u}_j}{\partial x_j} + \frac{\partial \overline{u'_i u'_j}}{\partial x_j} = \bar{u}_i \frac{\partial \bar{u}_j}{\partial x_j} + \bar{u}_j \frac{\partial \bar{u}_i}{\partial x_j} + \frac{\partial \overline{u'_i u'_j}}{\partial x_j} \\ \overline{\frac{\partial u_i u_j}{\partial x_j}} &= \bar{u}_j \frac{\partial \bar{u}_i}{\partial x_j} + \frac{\partial \overline{u'_i u'_j}}{\partial x_j}, \end{aligned} \tag{A.9}$$

this time making use of the fact that non-linear terms drop out, and the time-averaged continuity equation. Then, for the full momentum equation one arrives at:

$$\begin{aligned} \overline{\frac{\partial(\bar{u}_i + u'_i)}{\partial t}} + \bar{u}_j \frac{\partial \bar{u}_i}{\partial x_j} &= -\overline{\frac{1}{\rho_0} \frac{\partial(\bar{p} + p')}{\partial x_i}} - \overline{\frac{\bar{\rho} + \rho'}{\rho_0} g \delta_{i3}} + \overline{\frac{\partial}{\partial x_j} \left((\bar{\nu} + \nu') \frac{\partial(\bar{u}_i + u'_i)}{\partial x_j} \right)} - \frac{\partial \overline{u'_i u'_j}}{\partial x_j}, \\ \frac{\partial \bar{u}_i}{\partial t} + \bar{u}_j \frac{\partial \bar{u}_i}{\partial x_j} &= -\frac{1}{\rho_0} \frac{\partial \bar{p}}{\partial x_i} - \frac{\bar{\rho}}{\rho_0} g \delta_{i3} + \frac{\partial}{\partial x_j} \left(\bar{\nu} \frac{\partial \bar{u}_i}{\partial x_j} + \overline{\nu' \frac{\partial u'_i}{\partial x_j}} - \overline{u'_i u'_j} \right). \end{aligned} \tag{A.10}$$

The advection terms in the internal energy balance equation can be rewritten in a similar fashion:

$$u_j \frac{\partial T}{\partial x_j} = \frac{\partial u_j T}{\partial x_j} - T \frac{\partial u_j}{\partial x_j} = \frac{\partial u_j T}{\partial x_j}. \tag{A.11}$$

Analogously, decomposing and averaging yields:

$$\begin{aligned} \overline{\frac{\partial u_j T}{\partial x_j}} &= \frac{\overline{\partial(\bar{u}_j + u'_j)(\bar{T} + T')}}{\partial x_j} = \frac{\partial \bar{u}_j \bar{T}}{\partial x_j} + \frac{\partial \overline{u'_j T'}}{\partial x_j} = \bar{T} \frac{\partial \bar{u}_j}{\partial x_j} + \bar{u}_j \frac{\partial \bar{T}}{\partial x_j} + \frac{\partial \overline{u'_j T'}}{\partial x_j} \\ \overline{\frac{\partial u_j T}{\partial x_j}} &= \bar{u}_j \frac{\partial \bar{T}}{\partial x_j} + \frac{\partial \overline{u'_j T'}}{\partial x_j}. \end{aligned} \tag{A.12}$$

Then finally, the full time-averaged internal energy balance equation is obtained:

$$\begin{aligned} \overline{\frac{\partial(\bar{T} + T')}{\partial t}} + \overline{(\bar{u}_j + u'_j) \frac{\partial(\bar{T} + T')}{\partial x_j}} &= \overline{\frac{\partial}{\partial x_j} \left((\bar{\alpha} + \alpha') \frac{\partial(\bar{T} + T')}{\partial x_j} \right)} - \frac{\partial \overline{u'_j T'}}{\partial x_j}, \\ \frac{\partial \bar{T}}{\partial t} + \bar{u}_j \frac{\partial \bar{T}}{\partial x_j} &= \frac{\partial}{\partial x_j} \left(\bar{\alpha} \frac{\partial \bar{T}}{\partial x_j} + \overline{\alpha' \frac{\partial T'}{\partial x_j}} - \overline{u'_j T'} \right). \end{aligned} \tag{A.13}$$

In summary, the time averaged versions of the three simplified governing equations can be written as:

$$\frac{\partial \bar{u}_j}{\partial x_j} = 0, \tag{A.14}$$

$$\frac{\partial \bar{u}_i}{\partial t} + \bar{u}_j \frac{\partial \bar{u}_i}{\partial x_j} = -\frac{1}{\rho_0} \frac{\partial \bar{p}}{\partial x_i} - \frac{\bar{\rho}}{\rho_0} g \delta_{i3} + \frac{\partial}{\partial x_j} \left(\bar{\nu} \frac{\partial \bar{u}_i}{\partial x_j} + \overline{\nu' \frac{\partial u'_i}{\partial x_j}} - \overline{u'_i u'_j} \right), \tag{A.15}$$

$$\frac{\partial \bar{T}}{\partial t} + \bar{u}_j \frac{\partial \bar{T}}{\partial x_j} = \frac{\partial}{\partial x_j} \left(\bar{\alpha} \frac{\partial \bar{T}}{\partial x_j} + \overline{\alpha' \frac{\partial T'}{\partial x_j}} - \overline{u'_j T'} \right). \tag{A.16}$$

B

THERMOPHYSICAL PROPERTY DATA

This appendix gives an overview of the relevant thermophysical property data for water and methanol, along with the polynomial fits that are used in the code. All polynomials are of the form:

$$\Phi(T) = c_0 + c_1 T + c_2 T^2 + c_3 T^3, \tag{B.1}$$

with $\Phi(T)$ the instantaneous property value, and c_i the i-th coefficient for that property.

Coefficient c_i	Value (kg m^{-3} T^{-i})
c_0	$2.242424787000341 \times 10^2$
c_1	$6.845086004427072 \times 10^0$
c_2	$-1.900181943660245 \times 10^{-2}$
c_3	$1.588732481181044 \times 10^{-5}$

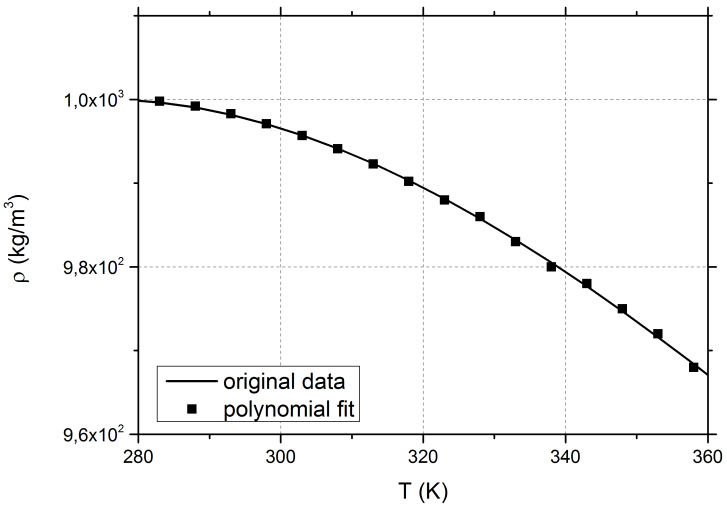

Table B.1: Polynomial coefficients, and plot of the original data and polynomial fit for density of water.

Coefficient c_i	Value ($m^2\ s^{-1}\ T^{-i}$)
c_0	$1.076696713851169 \times 10^{-4}$
c_1	$-9.175897694764074 \times 10^{-7}$
c_2	$2.627112569010185 \times 10^{-9}$
c_3	$-2.517546496359645 \times 10^{-12}$

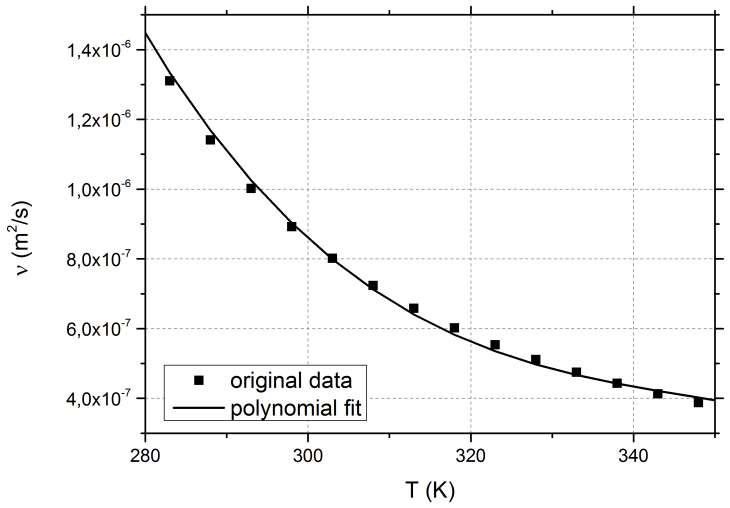

Table B.2: Polynomial coefficients, and plot of the original data and polynomial fit for kinematic viscosity of water.

Coefficient c_i	Value ($m^2\ s^{-1}\ T^{-i}$)
c_0	$-7.224677907875219 \times 10^{-7}$
c_1	$6.676866022270819 \times 10^{-9}$
c_2	$-1.712225792132925 \times 10^{-11}$
c_3	$1.506872127813015 \times 10^{-14}$

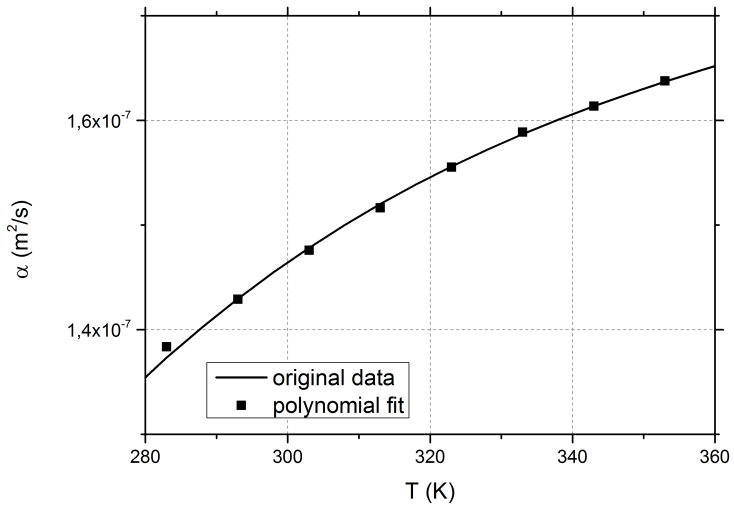

Table B.3: Polynomial coefficients, and plot of the original data and polynomial fit for thermal diffusivity of water.

Coefficient c_i	Value (kg m^{-3} T^{-i})
c_0	$9.445357371066286 \times 10^{2}$
c_1	$-2.448008207069267 \times 10^{-1}$
c_2	$-7.158362470866933 \times 10^{-4}$
c_3	$-7.527195027190587 \times 10^{-7}$

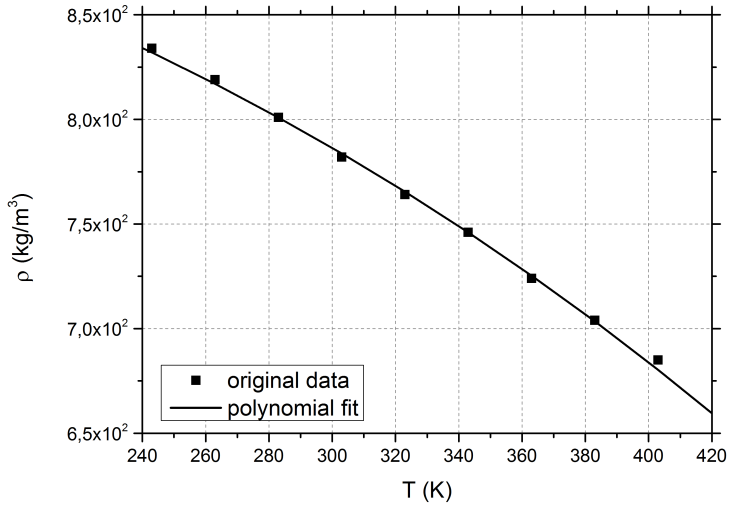

Table B.4: Polynomial coefficients, and plot of the original data and polynomial fit for density of methanol.

Coefficient c_i	Value (m^2 s^{-1} T^{-i})
c_0	$1.855700783682902 \times 10^{-5}$
c_1	$-1.360900531419995 \times 10^{-7}$
c_2	$3.430417121080055 \times 10^{-10}$
c_3	$-2.928785230868978 \times 10^{-13}$

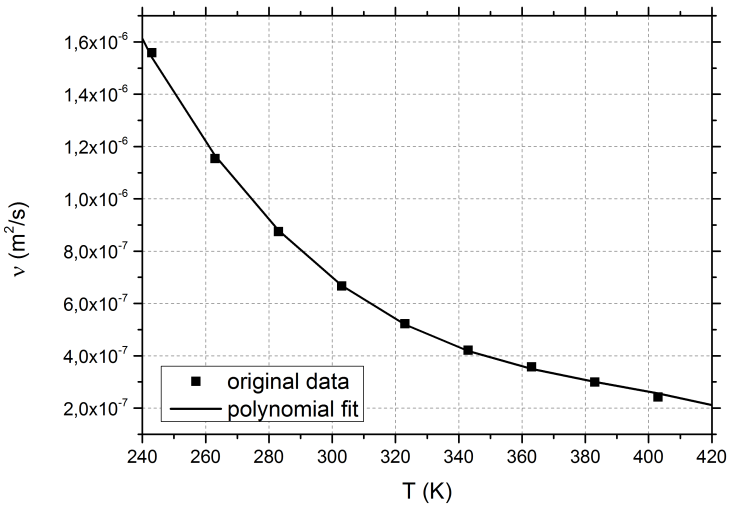

Table B.5: Polynomial coefficients, and plot of the original data and polynomial fit for kinematic viscosity of methanol.

Coefficient c_i	Value (m^2 s^{-1} T^{-i})
c_0	$1.469937007480173 \times 10^{-7}$
c_1	$1.146124340048872 \times 10^{-10}$
c_2	$-1.385753275022445 \times 10^{-12}$
c_3	$1.621148499744287 \times 10^{-15}$

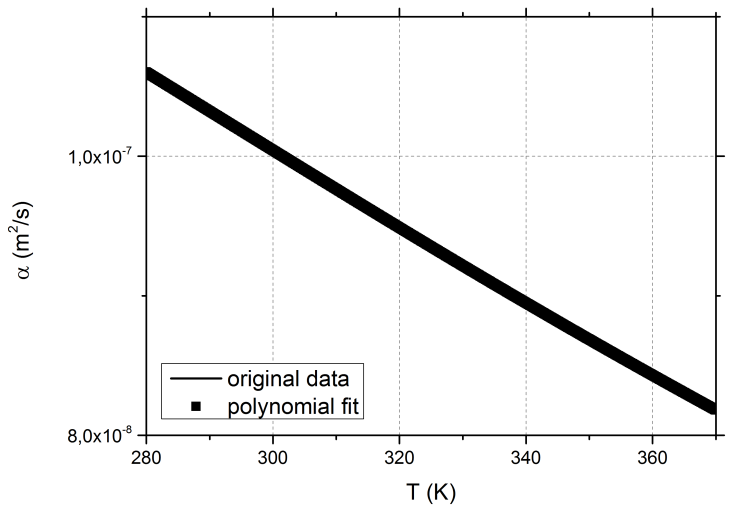

Table B.6: Polynomial coefficients, and plot of the original data and polynomial fit for thermal diffusivity of methanol.

BIBLIOGRAPHY

[1] *Supercritical-Water-Cooled Reactor (SCWR),* https://www.gen-4.org/gif/jcms/c_40679/technology-system-scwr, accessed: 08-07-2015.

[2] J. Yoo, *The turbulent flows of supercritical fluids with heat transfer,* Annual Review of Fluid Mechanics **45**, 495 (2013).

[3] L. Valencia, J. Pallares, I. Cuesta, and F. Grau, *Turbulent Rayleigh-Bénard convection of water in cubical cavities: a numerical and experimental study,* International Journal of Heat and Mass Transfer **50**, 3203 (2007).

[4] R. B. Bird, W. E. Stewart, and E. N. Lightfoot, *Transport Phenomena,* (Wiley, 1966) pp. 71–319.

[5] T. Poinsot and D. Veynante, *Theoretical and numerical combustion,* (R.T. Edwards, 2005) p. 22.

[6] A. Oberbeck, *Ueber die Wärmeleitung der Flüssigkeiten bei Berücksichtigung der Strömungen infolge von Temperaturdifferenzen,* Annalen der Physik **243**, 271 (1879).

[7] D. Gray and A. Giorgini, *The validity of the Boussinesq approximation for liquids and gases,* International Journal of Heat Mass Transfer **19**, 545 (1976).

[8] F. Nieuwstadt, *Turbulentie,* (Epsilon Uitgaven, 1998) pp. 137–138.

[9] H. Bénard, *Les tourbillons cellulaires dans une nappe liquide: propageant de la chaleur par convection en régime permanent,* Annales de Chimie et de Physique **23**, 62 (1901).

[10] J. W. Strutt Baron Rayleigh, *On convection currents in a horizontal layer of fluid, when the higher temperature is on the under side,* Scientific papers **6**, 1911 (1920).

[11] G. Ahlers, E. Brown, F. Araujo, D. Funfschilling, S. Grossmann, and D. Lohse, *Non-Oberbeck-Boussinesq effects in strongly turbulent Rayleigh-Bénard convection,* Journal of Fluid Mechanics **569**, 409 (2006).

[12] G. Ahlers, S. Grossmann, and D. Lohse, *Heat transfer and large scale dynamics in turbulent Rayleigh-Bénard convection,* Review of Modern Physics **81**, 503 (2009).

[13] S. Grossmann and D. Lohse, *Scaling in thermal convection: A unifying theory,* Journal of Fluid Mechanics **407**, 27 (2000).

[14] F. Busse, *Non-linear properties of thermal convection,* Reports on Progress in Physics **41**, 1929 (1978).

[15] J. Pallares, M. Arroyo, F. Grau, and F. Giralt, *Experimental laminar Rayleigh-Bénard convection in a cubical cavity and moderate Rayleigh and Prandtl numbers,* Experiments in Fluids **31**, 208 (2001).

[16] J. Pallares, I. Cuesta, and F. Grau, *Laminar and turbulent Rayleigh-Bénard convection in a perfectly conducting cubical cavity,* International Journal of Heat and Fluid Flow **23**, 346 (2002).

[17] L. Valencia, J. Pallares, I. Cuesta, and F. Grau, *Rayleigh-Bénard convection of water in a perfectly conducting cubical cavity: effects of temperature-dependent physical properties in laminar and turbulent regimes,* Numerical Heat Transfer **47:4**, 333 (2005).

[18] G. Ahlers, F. Araujo, D. Funfschilling, S. Grossmann, and D. Lohse, *Non-Oberbeck-Boussinesq effects in gaseous Rayleigh-Bénard convection,* Physical Review Letters **98**, (2007).

[19] K. Hanjalić, S. Kenjereŝ, M. Tummers, and H. Jonker, *Analysis and modeling of physical transport phenomena,* (VSSD, 2007) pp. 115–153.

[20] G. Grötzbach, *Spatial Resolution Requirements for Direct Numerical Simulation of the Rayleigh-Bénard convection,* Journal of Computational Physics **49**, 241 (1983).